



Master's Thesis

^{23}Na and ^{35}Cl NMR of saline solutions

Anita Karsa

Supervisor: Mónika Bokor
Senior Researcher
Wigner Research Centre for Physics
of the Hungarian Academy of Sciences

Co-supervisor: Ferenc Simon
Professor
BME Physics Department

Budapest University of Technology and Economics

2014.



Diplomamunka feladat a Fizikus mesterképzési (MSc) szak hallgatói számára

A hallgató neve: Karsa Anita	szakiránya: orvosi fizika
A diplomamunkát gondozó (a záróvizsgát szervező) tanszék:	Nukleáris Technika Tanszék

A diplomamunka készítésének helye: MTA Wigner FK	
A témavezető neve: Bokor Mónika	A konzulens neve: Simon Ferenc (külső témavezető esetén kijelölt tanszéki munkatárs)
– munkahelye: MTA Wigner FK, SZFI	– beosztása: Egyetemi tanár
– beosztása: Tudományos főmunkatárs	– e-mail címe: simon@esr.phy.bme.hu
– e-mail címe: bokor.monika@wigner.mta.hu	

A diplomamunka címe: NMR-érzékenység és kvantitatív analitika	azonosítója: DM-2013-74
A téma rövid leírása, a megoldandó legfontosabb feladatok felsorolása: Az élő szervezetekben zajló kémiai reakciók (pl. ligandum receptorhoz való kötődése, ion bekerülése az ioncsatornába, fehérje „feltekeredése”) általában a fehérje és az azt körülvevő oldószer közötti határfelületen történnek. A só ionok a fiziológiai rendszerek nélkülözhetetlen összetevői és így a fehérje-oldószer határfelület sem írható le a fehérje aminosav-oldalláncai és az ionok közötti kölcsönhatások figyelembe vétele nélkül. A hallgató feladata a fehérje-oldószer kölcsönhatás vizsgálatának szempontjából fontos oldatban egy kiválasztott rezonáns mag (pl. ^{23}Na) nagyfelbontású NMR-spektruma intenzitásának a mennyiségi meghatározása.	

A feladat kiadásának időpontja: **2013. február 5.**

Témavezető vagy tanszéki konzulens aláírása:	A diplomamunka témakiírását jóváhagyom (tanszékvezető aláírása):
--	---



Alulírott **Karsa Anita** a Budapesti Műszaki és Gazdaságtudományi Egyetem fizikus MSc szakos hallgatója kijelentem, hogy ezt a diplomamunkát meg nem engedett segédeszközök nélkül, önállóan, a témavezető irányításával készítettem, és csak a megadott forrásokat használtam fel.

Minden olyan részt, melyet szó szerint, vagy azonos értelemben, de átfogalmazva más forrásból vettem, a forrás megadásával jelöltem.

Budapest, 2014. június 2.

aláírás

Köszönetnyilvánítás

Szeretném megköszönni Bokor Mónikának, Tompa Kálmánnak és Simon Ferencnek a diplomamunkám vezetését. Remekül motiválták a munkámat és kérdéseimmel mindig fordulhattam hozzájuk.

Felbecsülhetetlen segítséget nyújtottak Bacsa Sándor, Horváth Béla és Kovács Tamás a mérésekhez szükséges eszközök elkészítésében és összerakásában.

Köszönöm Bokor Mónikának, Kamasa Pawelnek és Verebélyi Tamásnak, hogy eredményeiket felhasználhattam a dolgozatomban.

Köszönöm családomnak, barátaimnak és kedvesemnek az önzetlen és odaadó támogatást.

Financial support by the European Research Council Grant Nr. ERC-259374-Sylo is acknowledged.

Contents

1	Motivation	4
2	Introduction	6
2.1	Nuclear Magnetic Resonance	6
2.1.1	Nuclear magnetic resonance phenomenon	6
2.1.2	Signal detection	8
2.1.3	Pulse sequences	10
2.2	Interactions of quadrupole nuclei in solutions	13
2.2.1	The quadrupole interaction	16
2.3	Basics of NMR probes	17
2.3.1	Coil design	18
2.3.2	Circuit designs	18
3	Results and discussion	22
3.1	Development of high sensitivity probe	22
3.1.1	Coil design and circuit	22
3.1.2	Tuning of the circuit	23
3.1.3	Shimming	24
3.1.4	Temperature control	25
3.2	Spectrometer characterization	27
3.2.1	Output pulses	27
3.2.2	Signal detection	29
3.2.3	Noise figure	30
3.3	Quantitative study of NMR experiments	33
3.3.1	Calculation of circuit parameters	33
3.3.2	Calculation of bulk magnetization	35
3.4	Preliminary experiments on saline solutions	36

3.4.1	Analysis of T_1 and T_2 data	38
3.4.2	Results and discussion	39
3.4.3	Conclusion	43
3.5	Experiments on solutions with lysozyme	46
4	Summary and conclusions	50
	Appendices	52
A	The effect of a stationary water dipole on a quadrupole nucleus	52
B	Matlab code of signal and noise calculations	55
C	Optimization of C_T and C_M	59
C.1	Low frequency circuit	60
C.2	High frequency circuit	61
	Bibliography	62

Chapter 1

Motivation

Characterization of molecular dynamics in saline solutions is crucial while aiming for a thorough understanding of the properties and mechanisms of extra- and intracellular fluids in the human body. These substances of liquid state are saline solutions of about $100 \frac{mmol}{dm^3}$ concentration containing additional proteins, ions and glucose. The mechanisms characterizing the interactions between vital protein macromolecules and their saline surrounding are yet to be uncovered in detail. However, these processes are of great physiological importance. It would be significant to know whether minor changes in the concentration of the saline environment effect the physical and chemical properties of a protein or if it is still capable of maintaining its biological functionality.

The first step towards starting profound observations concerning a wide range of proteins is clarification of the properties of a saline solution without additional substances. Interactions between sodium ions, chlorine ions and water dipoles are considered to be of a long-distance, electrostatic nature. However, recent observations using various scientific methods implied short-distance, chemical relations [1]. According to Ref. 2, no evidence of ion pair formation was found so far. A hydrate shell model consistent with the NMR relaxation rates of many nuclei was presented in [3].

Nuclear Magnetic Resonance is one of the many ways how molecular properties can be observed. However, previous to this point these experiments usually singled out ^1H as the detected nucleus¹. On one hand, ^1H nuclei are excessively present in almost every solution and provide high signal which makes detection conveniently simple. On the other hand, additional molecular information could be extracted out of ^{23}Na and ^{35}Cl measurements regarding the eutectic phase or the hydrate shell. Moreover, interactions between ions and macromolecular surfaces are far more interesting than the study of water environment.

¹Neither ^{23}Na , nor ^{35}Cl are popular nuclei in NMR researches.

As a consequence, several recent studies focus on these processes. In Ref. 4, static and dynamic light scattering was used to investigate hydrodynamic interactions between chaotropic, kosmotropic salt ions and lysozyme. Simulations targeting the observation of molecular dynamics of Na^+ and Cl^- near a protein surface were introduced in [5]. Interactions between macromolecules and salt ions is heavily researched area with several models developed (e.g. Hofmeister series, salt ion partitioning model) [6, 7].

In this work, I wish to demonstrate not only that ^{23}Na and ^{35}Cl are worth of observation, but that it is possible to routinely perform temperature dependent NMR experiments on them. I propose the continuation of this work to be thorough examinations of both of the aforementioned nuclei in various biologically relevant solutions.

Chapter 2

Introduction

2.1 Nuclear Magnetic Resonance

NMR (Nuclear Magnetic Resonance) is a widely used spectroscopic method for studying materials and molecular physics¹. Nuclei in a magnetic field absorb and re-emit electromagnetic radiation. This is the nuclear magnetic resonance phenomenon. While the process is of a purely quantum physical nature, an equivalent classical representation exists.

2.1.1 Nuclear magnetic resonance phenomenon

In the classical representation, one might think of the magnetic moment of a nucleus as a vector of given magnitude ($\mathbf{M}(t)$). Interactions of this magnetic moment with its magnetic environment ($\mathbf{B}(t)$) are described by the Bloch-equations [8] (see equation 2.1). The macroscopic magnetization obeys the Larmor relation and precesses about any static magnetic field with which it is not collinear. In the presence of a static magnetic field in the direction of the z axis (B_0), the (angular) frequency (Larmor frequency) of the precession is given by $\omega_L = \gamma B_0$, where γ is the so-called gyromagnetic ratio unique to each isotope. Applying a rotating magnetic field perpendicular to the z axis will cause displacement of the magnetic moments from their equilibrium direction towards the $x - y$ plane (see figure 2.5). In NMR, short pulses of such magnetic fields of excitation are used to irradiate magnetic moments. The proceeding relaxation is then detected. This relaxation follows an exponential decay with characteristic time T_1 along the z axis and T_2

¹Combined with spatial information, NMR is a powerful, non-invasive imaging modality often applied in medical studies and diagnosis (MRI).

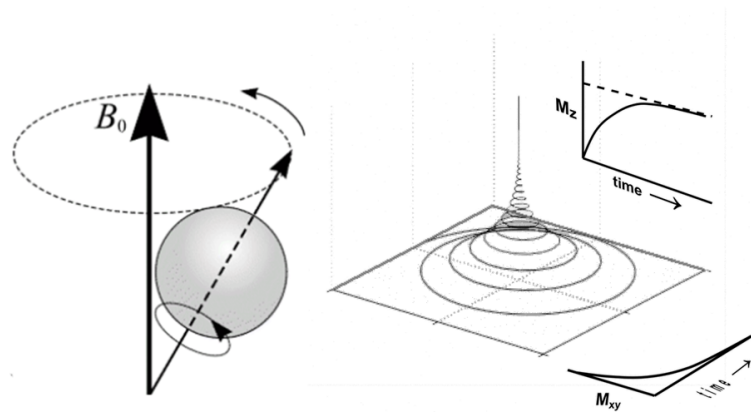


Figure 2.1: Precession and relaxation of a magnetic moment in presence of a static magnetic field B_0 , parallel to the z axis (sources: [9, 10])

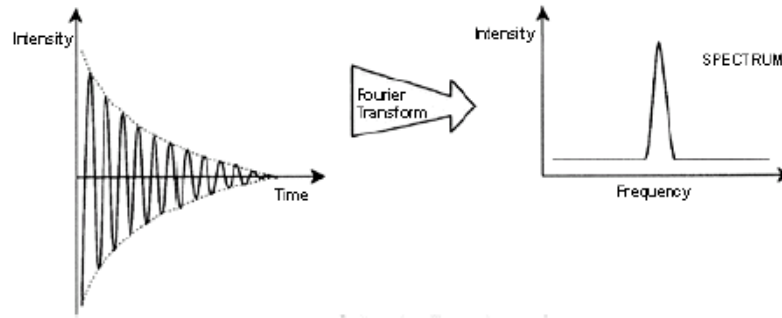


Figure 2.2: Typical NMR signal in time and frequency domains respectively (source: [11])

in the $x - y$ plane (see figure 2.1, on the right). The x and y components of the resultant magnetic moment is detected. Signals can be observed in time domain as well as in frequency domain. Since relaxation is exponential, in frequency domain a Lorentzian is expected. In case of off-resonance detection (see section 3.2.2), the signal is an oscillating function with an exponential envelope and the Lorentzian in frequency domain is shifted (see figure 2.2).

$$\begin{aligned}
 \frac{dM_x(t)}{dt} &= \gamma (\mathbf{M}(t) \times \mathbf{B}(t))_x - \frac{M_x(t)}{T_2} \\
 \frac{dM_y(t)}{dt} &= \gamma (\mathbf{M}(t) \times \mathbf{B}(t))_y - \frac{M_y(t)}{T_2} \\
 \frac{dM_z(t)}{dt} &= \gamma (\mathbf{M}(t) \times \mathbf{B}(t))_z - \frac{M_z(t) - M_0}{T_1}
 \end{aligned} \tag{2.1}$$

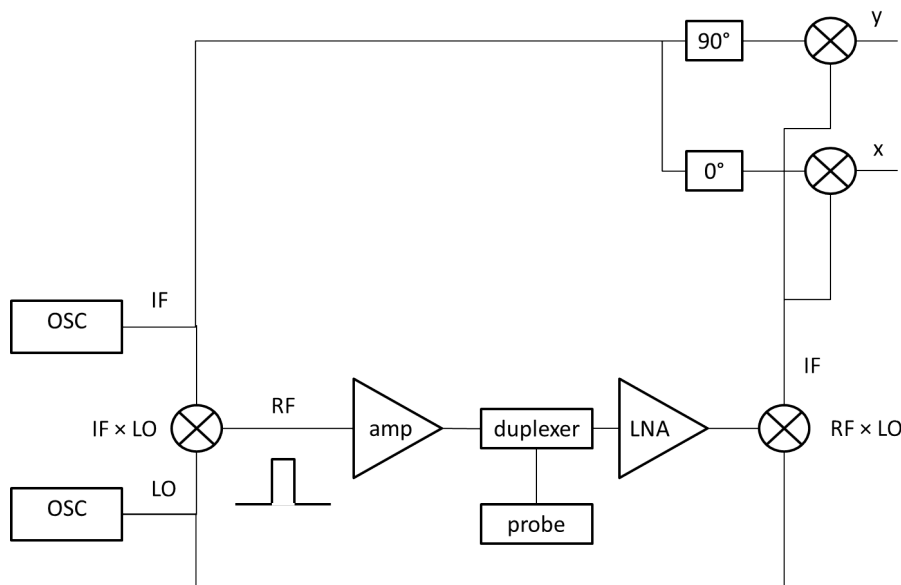


Figure 2.3: Bloch diagram of heterodyne NMR detection

2.1.2 Signal detection

In NMR, excitation and detection is performed by the transmitter and the receiver coils respectively [12]. The alternating magnetic field of excitation is induced by an alternating current applied to the transmitter coil. As the magnetic resonance phenomenon takes place (see section 2.1.1), due to the precessing magnetic moments, an alternating magnetization is present. This induces an alternating current in the receiver coil, which can be detected. Amplitude of the detected signal is proportional to the x and y component of the magnetization. In the most commonly used NMR configurations, the transmitter and the receiver coil is one and the same.

x and y components of the induced magnetization can be measured individually by heterodyne detection [12]. The principle is that of a vector voltmeter, where an excitation signal of given angular frequency ω (see equation 2.2) is applied on a system, which modulates its amplitude and shifts its phase (see equation 2.3). The output signal is then multiplied by the input signal (see equation 2.4). DC component of the resulting signal is identified as the x component ($B\cos(\phi)$) of the modulation. Applying a 90° phase shift to the initial signal (see equation 2.5) and repeating the aforementioned process (see equation 2.6) will provide the y component ($B\sin(\phi)$) of the modulation.

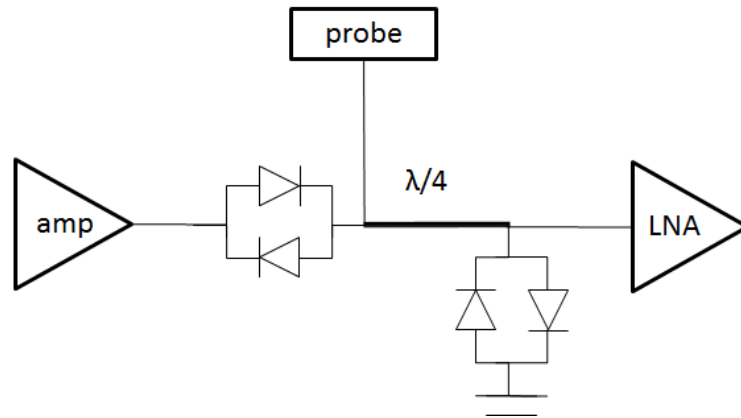


Figure 2.4: The NMR duplexer. The crossed diode pairs are short circuit for the emission and break during reception.

$$U_{in} = A \sin(\omega t) \quad (2.2)$$

$$U_{out} = B \sin(\omega t + \phi) \quad (2.3)$$

$$U_{in} \cdot U_{out} = \frac{AB}{2} \cdot (\cos(\phi) - \cos(2\omega t + \phi)) \quad (2.4)$$

$$U_{in90^\circ} = A \sin(\omega t - \frac{\pi}{2}) \quad (2.5)$$

$$U_{in90^\circ} \cdot U_{out} = \frac{AB}{2} \cdot \left(\sin(\phi) - \cos(2\omega t + \phi + \frac{\pi}{2}) \right) \quad (2.6)$$

Applying phase shift to a signal of arbitrary frequency is problematic. In the advanced technique of heterodyne detection (see figure 2.3), a signal of intermediate frequency (IF) is used. Phase shifts are applied only to signals of this particular frequency. First, the IF signal is multiplied by the signal of a local oscillator (LO), which is of arbitrary frequency. The two frequencies add up to an RF (Radio Frequency), which also equals to the Larmor frequency. The resulting signal is then applied to the sample. The output signal is first multiplied by the signal of the local oscillator resulting in a signal of the intermediate frequency on which the aforementioned vector voltmeter principle can be used.

An additional aspect of detection is that for excitation, high voltage pulses ($70 V$) are used, whereas detected signals are of small amplitudes ($1 \mu V$). In order to protect the detector from high power during pulses, NMR spectrometers are equipped with a duplexer [13] (see figure 2.4). During high power pulses from the amplifier, the diodes are passable and the excitation signal is transmitted towards the probe. However, the low noise amplifier (LNA) is protected by another pair of diodes. Low signals leaving the probe cannot open the diodes, therefore the signal reaches the LNA and is detected.

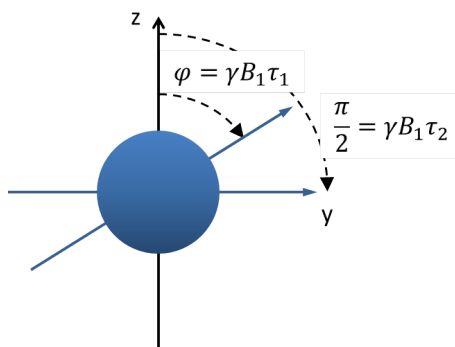


Figure 2.5: Effect of Rabi precession on a single nucleus

2.1.3 Pulse sequences

An alternating magnetic field of excitation (B_1) displaces magnetic moments out of their equilibrium (see section 2.1.1). If it is resonant with the Larmor frequency of the nucleus (which is necessary in order to rotate the magnetic moments), angular frequency of the displacement process is the so-called Rabi frequency given by $\omega_R = \gamma B_1$. Depending on the duration of the application of B_1 (in other words the duration of the pulse), magnetic moments will be flipped to different extents (see figure 2.5). A pulse that displaces the magnetic moments by ϕ is a ϕ -pulse and ϕ is called the flip angle. Pulse sequences [14] consist of a series of pulses with varying durations. This section focuses on demonstrating pulse sequences commonly used in NMR experiments.

Free Induction Decay

FID (Free Induction Decay) sequence consists of a single $\frac{\pi}{2}$ -pulse, which rotates magnetic moments by 90° . Characteristic time of the following exponential decay is T_2^* . Note that in the case of liquid samples, this imminent decay is due to the inhomogeneities of the static magnetic field rather than the irreversible spin-spin relaxation described by T_2 in the Bloch-equations (see section 2.1.1). In reality, the vector sum of individual magnetic moments is detected. Larmor frequency inhomogeneities (induced by magnetic field inhomogeneities) will cause a rapid decoherence of the moments which is usually much faster than the spin-spin relaxation of the individual spins (see figure 2.6). Width of the Lorentzian in spectral domain is therefore characteristic to the inhomogeneity of the static magnetic field for liquid samples².

²In solid state NMR, other factors are more dominant.

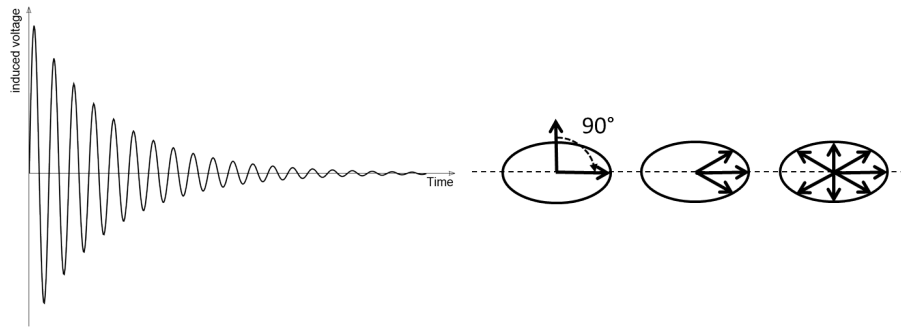


Figure 2.6: Free Induction Decay and decoherence of magnetic moments (source: [15])

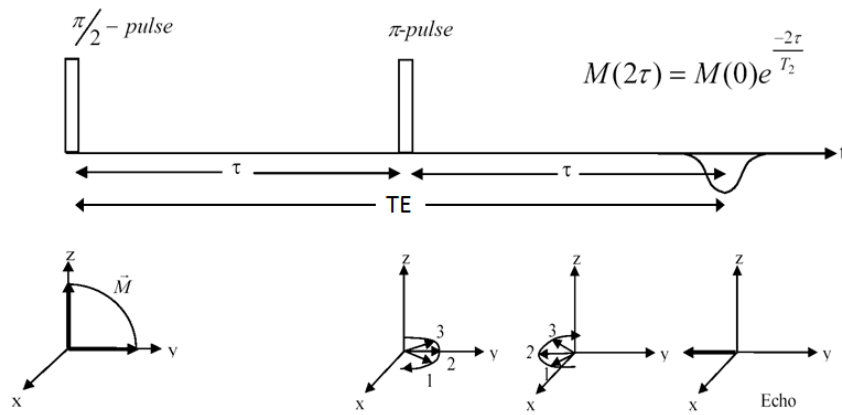


Figure 2.7: Rephasing property of the Spin Echo sequence

Spin Echo

In case of a FID, detection ideally starts right after the end of the $\frac{\pi}{2} - pulse$. In reality however, due to the strong difference in power between the pulse and the resulting signal (see section 3.2.2), detection is delayed by a considerable amount of dead time. This makes the initial value of the signal or its precise shape hard to determine. Fortunately, decoherence is a process that can be reversed by applying a $\pi - pulse$ (see figure 2.7). At TE (Echo Time), complete refocusing occurs and a detectable signal appears with definite shape and amplitude. Note that during the Spin Echo sequence, T_2 relaxation is inevitable, therefore the amplitude of the echo is always smaller than that of the FID. Spin Echo sequence is not suited for the detection of feeble signals.

Carl-Purcell-Meiboom-Gill sequence

The CPMG (Carl-Purcell-Meiboom-Gill) sequence is applicable for experiments targeting the measurement of T_2 . After the initial excitation with a $\frac{\pi}{2} - pulse$, a series of $\pi - pulses$

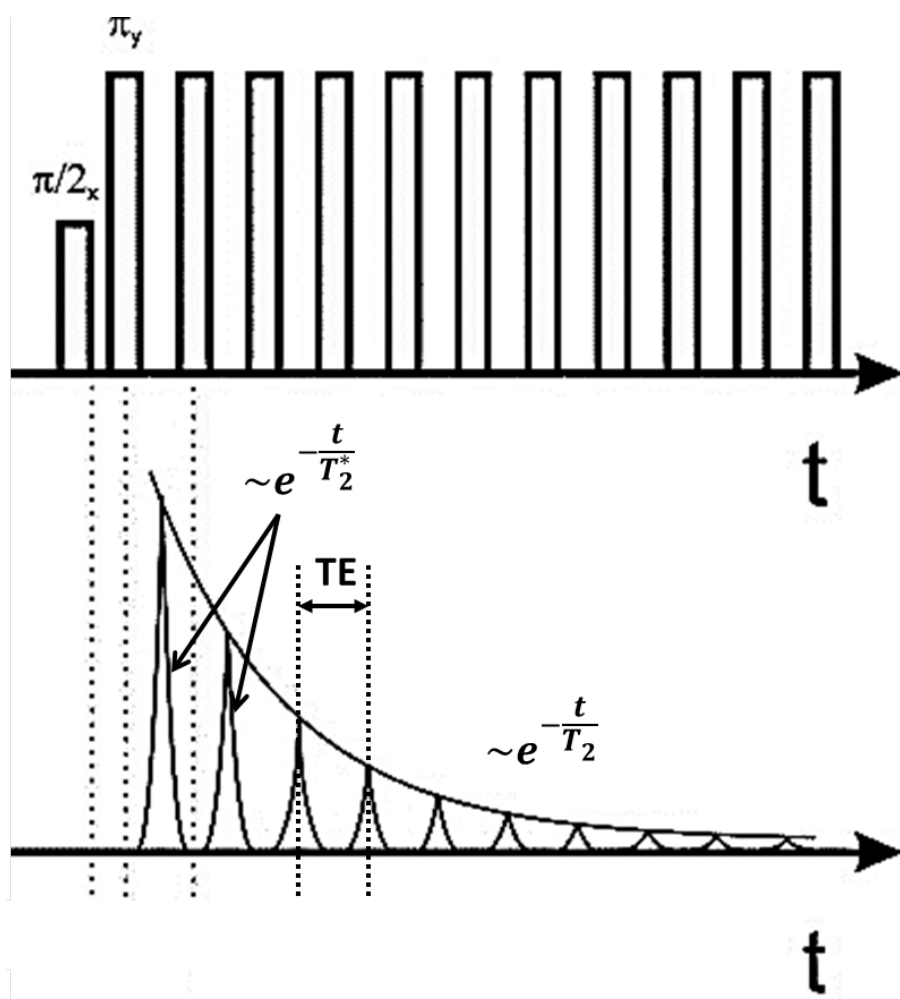


Figure 2.8: CPMG sequence for measuring T_2 (source: [16])

is applied in order to rephase magnetic moments³. After every rephasing period another decoherence will occur (with characteristic time T_2^*). Amplitude of the echos will decay exponentially due to the irreversible, always present T_2 relaxation (see figure 2.8).

Inversion Recovery

An IR (Inversion Recovery) sequence allows us to measure the so-called spin-lattice relaxation time, T_1 (see section 2.1.1). First, all magnetic moments are flipped by a π – pulse. After a considerable amount of time (τ), which allows for spin-lattice relaxation to partially take place, a $\frac{\pi}{2}$ – pulse is applied in order to rotate the remaining magnetization by 90° , placing it in the $x - y$ plane (see figure 2.9). This will result in a FID signal with amplitude dependent on τ . Repeating the experiment using different τ values will enable

³In this case, π – pulses are applied in the y direction instead of the x direction, thus every echo amplitude will be positive.

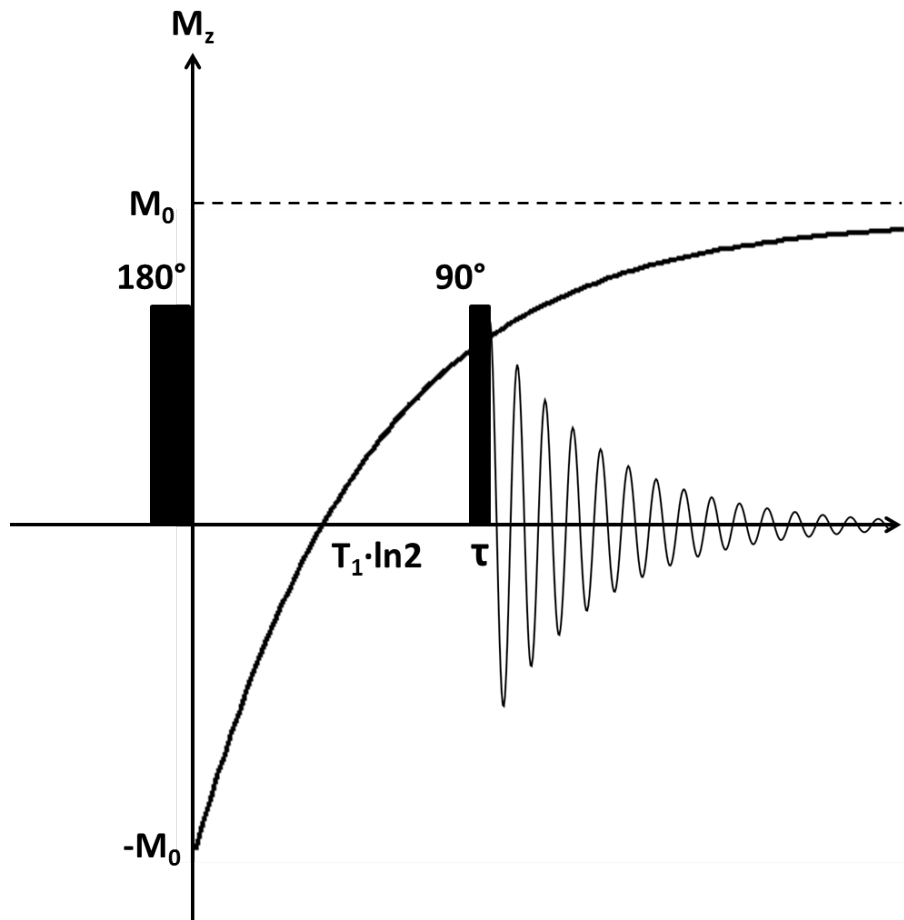


Figure 2.9: IR sequence for measuring T_1

us to fit an exponential to the amplitudes. As T_1 is by definition the characteristic time of the relaxation along the z axis, the resulting exponential will be of characteristic time T_1 .

2.2 Interactions of quadrupole nuclei in solutions

Although the classical model of excitation and relaxation (see section 2.1.1) is applicable in most cases, in reality nuclear magnetism is of a purely quantum mechanical nature. Nuclear dipoles ($\hat{\boldsymbol{\mu}}$) are coupled to nuclear spins [8] ($\hat{\mathbf{I}}$) (see equation 2.7), which are fundamental characteristics of nuclei. Hamiltonian of a nucleus in magnetic field is described by the so-called Zeeman Hamiltonian (see equation 2.8).

$$\hat{\boldsymbol{\mu}} = \gamma \hbar \hat{\mathbf{I}} \quad (2.7)$$

$$H_{Zeeman} = -\hat{\boldsymbol{\mu}} \cdot \mathbf{B} = -\gamma\hbar\hat{\mathbf{I}} \cdot \mathbf{B} \quad (2.8)$$

Different spin states correspond to different energy levels. For example, in case of a homogeneous magnetic field along the z axis (B_0), energy levels are described by equation 2.9 with m taking values from $\{-I, (-I+1)\dots(I-1), I\}$. Transition between two consecutive states is possible (given that the selection rule is $\Delta m = \pm 1$). During a transition, a photon of energy $\gamma\hbar B$ is either absorbed or emitted⁴.

$$E_m = -\gamma\hbar B_0 m \quad (2.9)$$

In general, interactions responsible for excitation and relaxation processes can be packed into a single Hamiltonian according to equation 2.10 (individual terms will be defined later).

$$H_{interactions} = H_Z + H_{RF} + H_\sigma + H_K + H_s + H_{DD} + H_J + H_Q \quad (2.10)$$

The Hamiltonian of the system determines the energy levels of a nucleus taking part in the interactions. Without excitation, the energy levels are populated according to the Boltzmann distribution $N_m \propto e^{-\frac{E_m}{k_B T}}$, where k_B and T are the Boltzmann constant and the temperature respectively [17]. During excitation, nuclei in the lower energy states will absorb the energy of the excitation field and flip to a higher energy state. Spin-lattice relaxation (T_1 , see section 2.1) means that equilibrium will be achieved by nuclei of the higher levels emitting energy due to one of the relaxation interactions in equation 2.10. T_1 can be expressed using the possible energy levels and the corresponding transition probabilities [17] (W_{mn} , see equation 2.11).

$$\frac{1}{T_1} = \frac{1}{2} \frac{\sum_{m,n} W_{mn} (E_m - E_n)^2}{\sum_n E_n^2} \quad (2.11)$$

$$W_{mn} = \frac{2\pi}{\hbar} \left| \langle m | \hat{\mathbf{V}} | n \rangle \right|^2 \delta(E_m - E_n) \quad (2.12)$$

Transition probabilities are given by Fermi's golden rule (see equation 2.12), where $\langle m |$ and $| n \rangle$ are the initial and final states of the transition and Dirac delta function (δ) expresses the energy conservation. $\hat{\mathbf{V}}$ is the Hamiltonian of the interaction⁵. Contribution

⁴ $\gamma B = \omega_L$ is the Larmor frequency. This is the quantum mechanical representation of the fact that a nucleus has to be irradiated by a signal of Larmor frequency.

⁵Considering the interactions separately, each is a possible relaxation channel. The more and the stronger these interactions are, the faster spin-lattice relaxation will occur.

of different interactions (in equation 2.10) to the overall relaxation rate is discussed in the next couple of sections.

H_Z and H_{RF}

Different interactions usually correspond to magnetic fields of different origins or characteristics. One of the basic components are H_Z (see equation 2.13), which is a Zeeman Hamiltonian assuming a homogeneous magnetic field (B_0). Applying this strong field generates different energy levels. The other main component is H_{RF} (see equation 2.14), which denotes the Hamiltonian of the irradiation.

$$H_Z = -\gamma\hbar\hat{\mathbf{I}} \cdot \mathbf{B}_0 \quad (2.13)$$

$$H_{RF} = -\gamma\hbar\hat{\mathbf{I}} \cdot \mathbf{B}_1(i \cdot \cos(\omega t) - j \cdot \sin(\omega t)) \quad (2.14)$$

H_σ , H_s and H_K

H_σ , H_s and H_K are the chemical shift (see 2.15), susceptibility shift (see 2.16) and Knight-shift (see 2.17) components respectively [17]. σ , s and K are tensors. The effect of these terms can be viewed as small, local and anisotropic deviations from the main homogeneous field.

$$H_\sigma = -\gamma\hbar\hat{\mathbf{I}} \cdot \sigma\mathbf{B}_0 \quad (2.15)$$

$$H_s = -\gamma\hbar\hat{\mathbf{I}} \cdot s\mathbf{B}_0 \quad (2.16)$$

$$H_K = -\gamma\hbar\hat{\mathbf{I}} \cdot K\mathbf{B}_0 \quad (2.17)$$

Chemical shift is caused by the net magnetic field contribution of a certain chemical environment surrounding the nucleus. For example, a given nucleus resonates at different frequencies in water or fat environment.

Susceptibility shift occurs due to volume magnetic susceptibility, which alters the magnetic field forming within a sample compared to the external magnetic field.

In metallic environment, the observed shift reflects the local magnetic field produced by the conduction electrons.

Our samples are saline solutions with homogeneous chemical environment, low and also homogeneous susceptibility and a lack of cohesive metallic environment, therefore these effects are not present.

H_{DD} and H_J

Dipole-dipole coupling (dipolar coupling) and J-coupling (indirect dipole dipole coupling) are interactions originating from nuclei generating local magnetic fields at each others positions [8]. In case of direct dipolar interactions (H_{DD}), nuclei are directly coupled to each other, while in case of J-coupling (H_J), at least one intermediate electron is involved. In presence of any spin motion, nuclei experience a time average of these spatial interactions which leads to motional narrowing and the effect of dipolar coupling is not observed, just like in case of our liquid solutions. J-coupling is observable only in high resolution NMR experiments.

2.2.1 The quadrupole interaction

In case of nuclei of spin larger then $1/2$, the effect mainly responsible for relaxation is the so-called quadrupole interaction (H_Q). In our case, this term is the one mainly responsible for relaxation. A nucleus representing a spatial charge distribution of $\rho(\mathbf{r})$ in an electric potential $V(\mathbf{r})$ will have an electrostatic energy of $E = \int \rho(\mathbf{r})V(\mathbf{r})\mathbf{dr}$ which will obviously contribute to the overall Hamiltonian. Since $\rho(\mathbf{r})$ is localized to the nucleus in which volume the electric potential is slowly varying, $V(\mathbf{r})$ can be expanded in a Taylor's series about the origin. The highest order term which neither does vanish and nor is a constant is the second order, quadrupole term. This will result in an extra term (H_Q , see equation 2.18, where Q is the quadrupole tensor and the final expression is valid only in principal axis system) in the overall Hamiltonian [17].

$$H_Q = \frac{1}{6} \sum_{\alpha,\beta} V_{\alpha\beta} Q_{\alpha\beta} = \frac{eQ\partial_z^2 V}{4I(2I-1)} \left\{ (3I_z^2 - I^2) + \frac{\partial_x^2 V - \partial_y^2 V}{\partial_z^2 V} (I_x^2 - I_y^2) \right\} \quad (2.18)$$

T_1 and T_2

In general, effects causing relaxation can be expressed in terms of a fluctuating, local magnetic field [17] (see equation 2.19, where $h_q(t)$ is the q component of the local field deviation and τ_c is the correlation time given by $\tau_c = \tau_\infty e^{\frac{E}{k_B T}}$). In these terms, T_1 and T_2 are given by equations 2.20 and 2.21.

$$\overline{h_q(t)h_q(t+\tau)} = h_q^2 \cdot e^{-\frac{|\tau|}{\tau_c}} \quad (2.19)$$

$$\frac{1}{T_1} = \gamma^2 (h_x^2 + h_y^2) \frac{\tau_c}{1 + \omega_L \tau_c} \quad (2.20)$$

$$\frac{1}{T_2} = \gamma^2 h_z^2 \tau_c + \frac{1}{2T_1} \quad (2.21)$$

If $h_x^2 = h_y^2 = h_z^2$, in other words if the interactions responsible for the relaxation are statistically anisotropic and $\omega_L \cdot \tau_c \ll 1$, T_1 equals T_2 . Moreover, T_2 can be expressed by equation 2.22, where $\langle \omega^2 \rangle$ is the second moment of the Larmor frequency fluctuations [18]. The average is taken over the resonating spins.

$$\frac{1}{T_2} = \langle \omega^2 \rangle \tau_c \quad (2.22)$$

According to Ref. 19, quadrupole interaction of $I = 3/2$ nuclei leads to the following relaxation rates, h is the Planck-constant and e is the elementary charge.

$$\frac{1}{T_1} = \frac{1}{T_2} = \frac{2\pi^2}{5} \left(\frac{eQ\partial_z^2 V}{h} \right)^2 \tau_c \quad (2.23)$$

Expression 2.23 shows that in case of nuclei with large quadrupole moments, an asymmetric electrostatic environment induces an immediate widening⁶ of the spectrum ($\Delta f = \frac{1}{\pi \cdot T_2}$ is the linewidth in spectrum domain). That said, the signal is expected to remain detectable while quadrupole ions are in a solute environment and it will presumably vanish at the solid state, where the lack of molecular motion induces highly asymmetrical surroundings.

Appendix A. demonstrates a simple discussion about the effect a stationary water dipole has on the signal width.

2.3 Basics of NMR probes

The probe plays an important role in NMR experiments since it is responsible for signal transmission and detection. It was a substantial part of this thesis to construct a probe for the measurements. Initial magnetization of the sample is given by equation 2.24, where N is the number of nuclei in the sample and I is the spin. NMR signal is given by

⁶Temperature dependence of τ_c also induces line broadening, but in case of the quadrupole interaction, $\partial_z^2 V$ is the term mainly responsible for it.

equation 2.25 [14], where $\mathcal{B}(\mathbf{r})$ is the laboratory frame magnetic field at location \mathbf{r} produced by a hypothetical unit current flowing in the coil and $\mathbf{M}(\mathbf{r}, \mathbf{t})$ is the time dependent magnetization density. In the final expression $\eta = \frac{V_{sample}}{V_{coil}}$ is the so-called filling factor. In case of low signals (due to low Larmor frequency, low abundance or low concentration) the use of a high sensitivity probe can be crucial. There are two important points of the circuit in relation to sensitivity. One of them is the coil design and the other is effective energy transmission.

$$M_0 = N \frac{\gamma^2 \hbar^2 I(I+1) B_0}{3k_B T} \quad (2.24)$$

$$\begin{aligned} S &= -\partial_t \int_{sample} \mathcal{B}(\mathbf{r}) \cdot \mathbf{M}(\mathbf{r}, \mathbf{t}) d\mathbf{r} \\ &\propto N \cdot \omega_L^2 \cdot \eta \cdot I(I+1) \cdot \frac{1}{T} \end{aligned} \quad (2.25)$$

2.3.1 Coil design

In liquid NMR, usually a cylindrical saddle coil design (see figure 2.10, b) is adopted [20]. This guarantees a highly homogeneous, transverse magnetic field of excitation while allowing axial access (efficient way of introducing a sample without altering the configuration of the probe in the magnet). Unfortunately, small scale implementation of such a coil is extremely difficult.

Another possibility is using a solenoid (see figure 2.10, a), in which case implementation is relatively easy. However, a solenoid with low inductance (thus optimized for effective transmission, see section 2.3.2) consists of only a few turns, which might result in low B_1 homogeneity and signal loss.

2.3.2 Circuit designs

The NMR device consists of a magnet, pre-amplifier and spectrometer (see figure 2.11). Signals of excitation and detection are carried to and from the probe via a standard BNC cable with an impedance of 50Ω . In order to successfully transmit signals to and from the probe, its resultant impedance has to be matched with $(50+0i) \Omega$. The simplest implementation of such a probe is a circuit of a coil and two tunable capacitors⁷ [21] (see

⁷Both the real and the imaginary part of the impedance has to be matched. Therefore at least two tunable parameters are necessary.

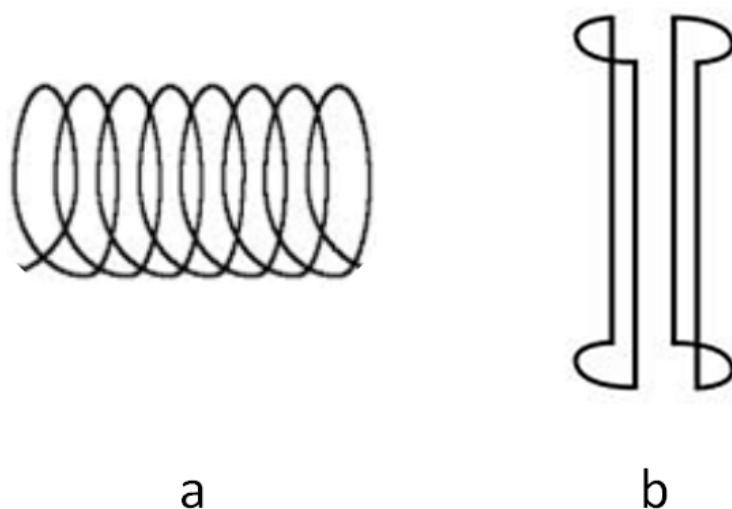


Figure 2.10: RF and receiver coil designs: a solenoid (left) and a saddle coil (right)

figure 2.12, a). This configuration is applicable to low Larmor frequency nuclei (up to 150 MHz , which is just above the Larmor frequency of ^{21}P in case of a 7 T magnet).

For higher frequencies, the appropriate capacitance and impedance values become hard to implement. In this case a slightly different circuit configuration is suggested (see figure 2.12, b).

A short discussion on circuit parameter optimization can be found in Appendix C.

Coil impedance

In order to achieve high signal-to-noise ratio (SNR), filling factor should be maximized and thus the dimensions of the coil should be matched with the dimensions of the sample. Inductance of the coil can be slightly tuned by the number of turns. In case of a complex circuit, voltage on the elements is not necessarily less than the initial voltage (in figure 2.13 absolute value of the *coil - tuning capacitor parallel impedance* (denoted by Z) is much larger than the resultant $50\ \Omega$). High voltage gain leads to short RF pulses. For achieving a considerably high voltage gain $L \cdot \omega = 50\ \Omega$ is an applicable rule of thumb.

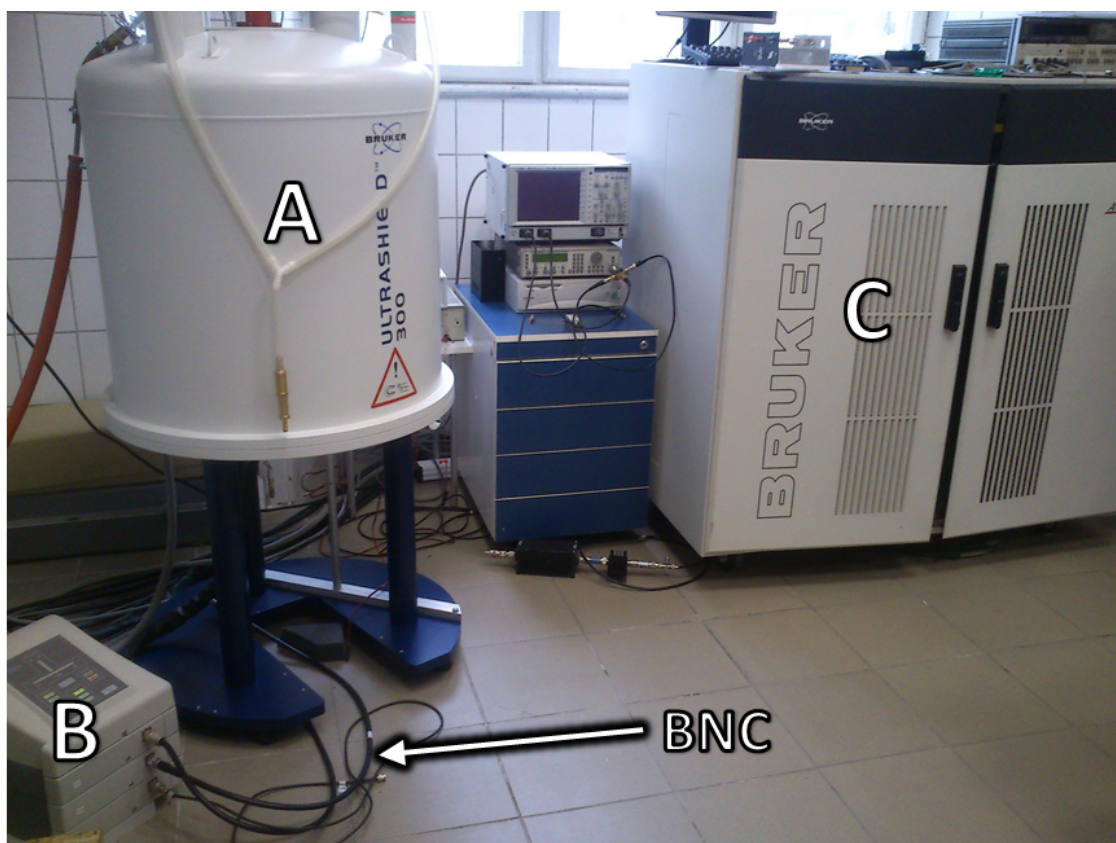


Figure 2.11: The Bruker 300 NMR system in operation. A: Magnet, B: Pre-amplifier, C: Spectrometer

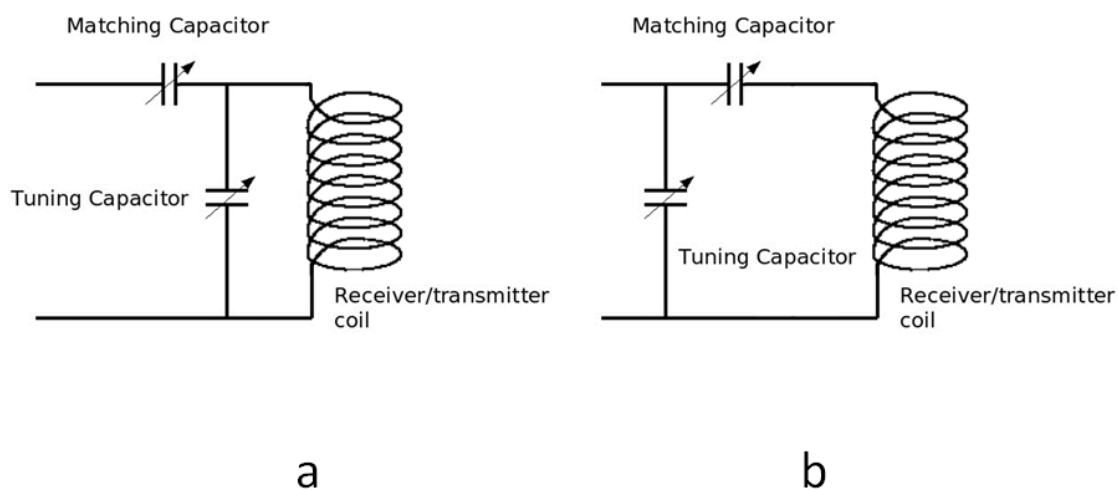


Figure 2.12: Circuit designs for different frequency ranges: for lower frequencies (left) and for higher frequencies (right)

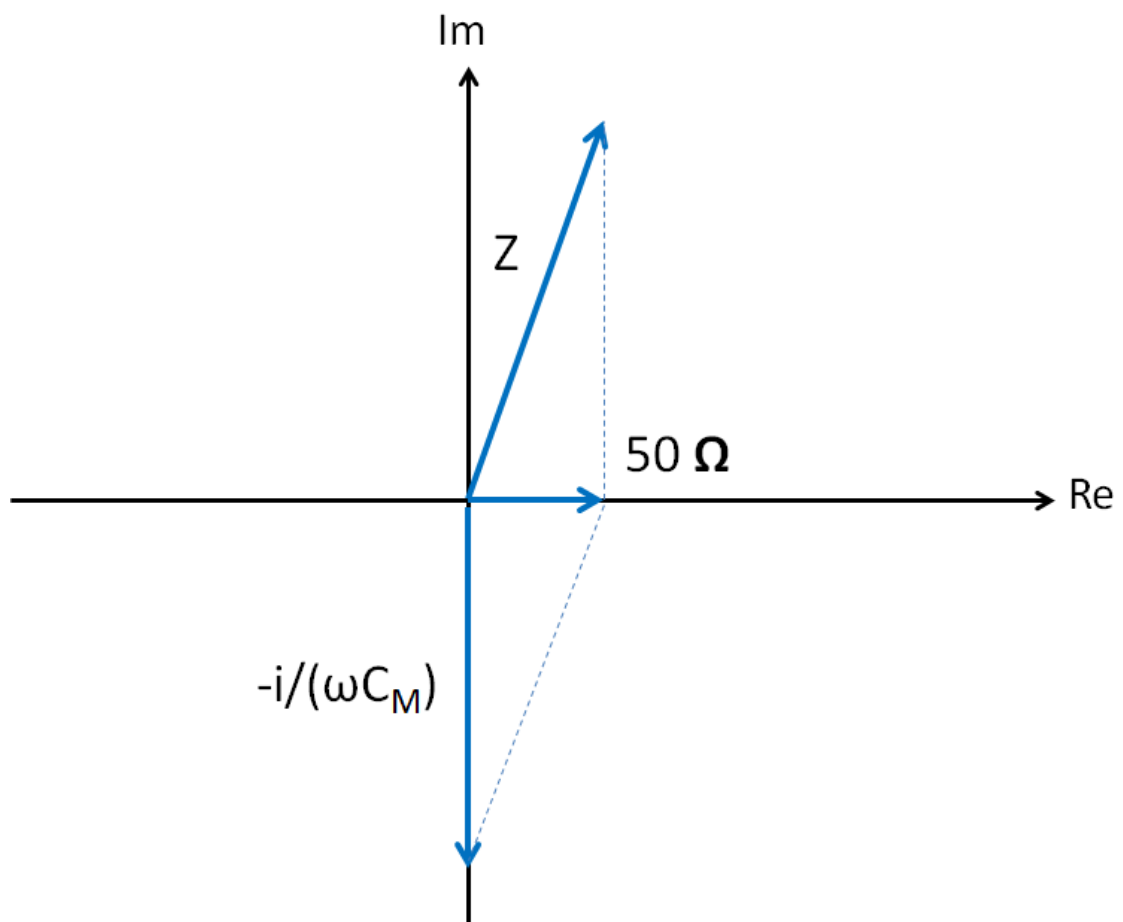


Figure 2.13: Construction of the 50Ω resultant impedance shows voltage gain on the receiver/transmitter coil

Chapter 3

Results and discussion

3.1 Development of high sensitivity probe

In case of low Larmor frequency nuclei, signal detection can become difficult as $S \propto \omega_L^2$ (see equation 2.25). A low concentration of the observed nuclei¹ further aggravates the problem. In this section, a possible way of achieving relatively high sensitivity is demonstrated. There are two important points of the circuit in relation to sensitivity. One of them is the coil design (maximizing filling factor and B_1 homogeneity) and the other is effective energy transmission (a tunable probe). Note that commercial solutions are usually optimized for easy handling and rapid sample exchange. These requirements are however not demanded in our case.

3.1.1 Coil design and circuit

In order to improve sensitivity through an increased filling factor, a solenoidal coil design is used, where the dimensions of the coil are matched with the dimensions of the sample. In order to achieve high energy transmission between the coil and the circuit input, $L \cdot \omega \approx 50 \Omega$ is a practicable rule of thumb. This means however that in case of a fix sample holder size (cylinder of diameter 5 mm and length 1 cm in our case), the optimal coil consists of about 10 turns. The B_1 magnetic field of a solenoid coil of 10 turns may become highly inhomogeneous, which would cause a decrease in signal amplitude. According to our experience, filling factor is more important at the scale of the size of our samples. Preliminary attempts with saddle coils did not show any improvements in

¹Biologically relevant saline concentration is about $150 \frac{\text{mmol}}{\text{dm}^3}$, which is the average value of the extra- and intracellular fluids of the human body. This means that the number of protons is approximately 370 times the number of ^{23}Na or ^{35}Cl ions.



Figure 3.1: The constructed NMR probe for broadband, low frequency measurements

signal amplitude or shape compared to experiments performed with carefully constructed solenoids. However, its implementation is considerably more difficult. Therefore, the solenoid concept was adapted.

The circuit is of the simplest possible design (see section 2.3) consisting of a receiver/transmitter coil and two tunable capacitors (see figure 3.1 upper). Later on a Teflon bracket was installed which serves to hold the coil in place and improve reproducibility of experiments (see figure 3.1 lower).

3.1.2 Tuning of the circuit

Tuning is one of the important steps of an NMR experiment. The probe is usually connected to the spectrometer via a BNC with a wave impedance of 50Ω . In order to achieve a maximal transmission of energy at the junction between the BNC and the probe,

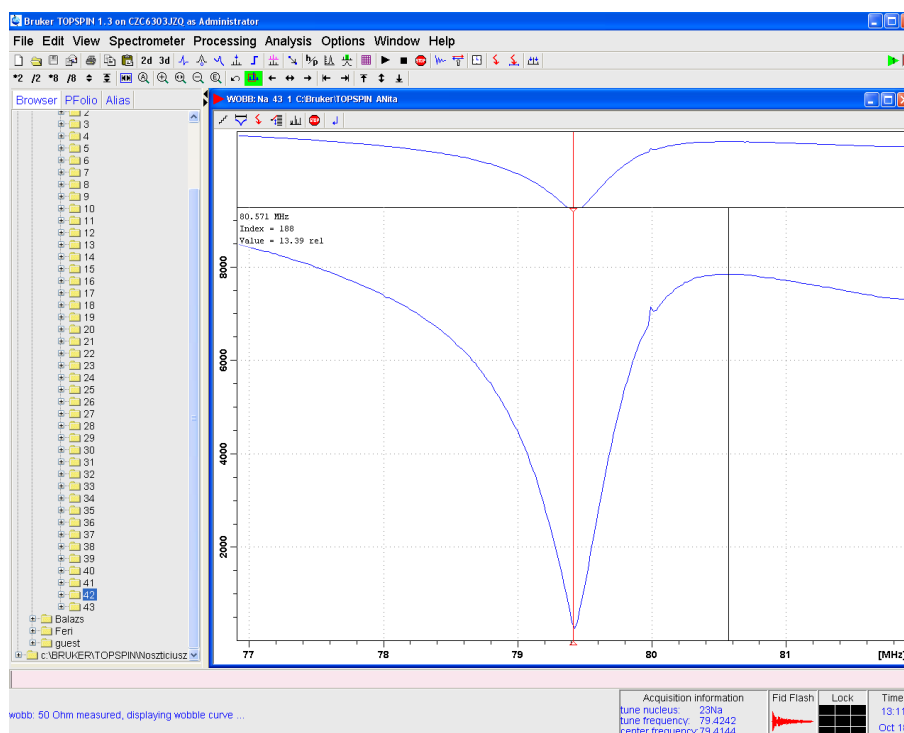


Figure 3.2: Tuning curve of an NMR probe. Note that zero reflection signal corresponds to an optimally tuned (and matched) probehead.

the resultant impedance of the circuit has to equal to 50Ω . This is implemented by using the tunable capacitors.

Our circuit is dedicated for broadband, low frequency experiments and thus is tunable between 25 MHz and 100 MHz . This provides a wide range of detectable nuclei. In case of our saline solutions both ^{23}Na (79.35 MHz at 7 T) and ^{35}Cl (29.4 MHz at 7 T) are observable. The tuning and matching capacitors are adjustable from outside of the magnet using stainless steel sticks soldered to them. Reflexion curve of a well-tuned circuit is seen in figure 3.2.

3.1.3 Shimming

For high resolution NMR spectroscopy, a relatively high homogeneity of the static magnetic field is necessary. This provides a similar homogeneity of the spatial distribution of Larmor frequencies and therefore a narrow spectrum, which leads to high resolution. The static magnetic field is on one hand never completely homogeneous and on the other hand small perturbations (such as introducing a probe) can considerably alter its structure. Shimming coils create magnetic fields along the z axis with spatially inhomogeneous magnitude, namely magnetic field gradients, in order to compensate for these inhomogeneities

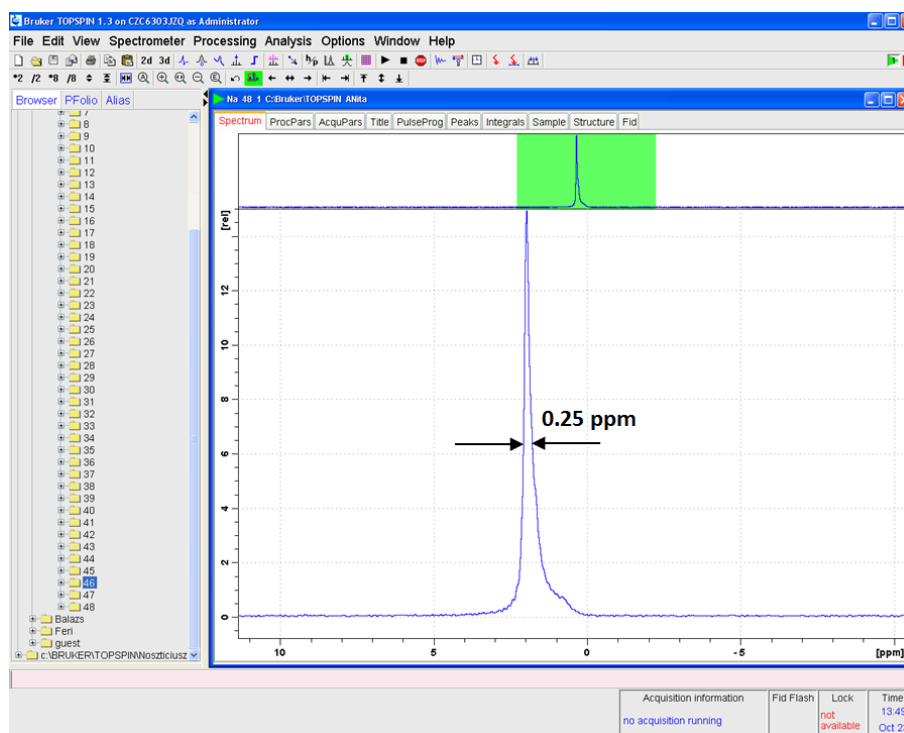


Figure 3.3: Screenshot of a well shimmed NMR signal. Note the very narrow (0.25 ppm) linewidth of the ^{23}Na signal. Without shimming linewidth is about $1\text{--}2\text{ ppm}$.

and improve resolution. Our system is equipped with 20 gradient coils (see figure 3.3). The experiments were performed with an approximately $0.3\text{--}0.4\text{ ppm}^{(2)}$ initial (on room temperature) width. In our case, shimming is also important regarding the fact that by lowering temperature the spectrum becomes considerably wider and the spectrum bandwidth is limited. In order to detect NMR signals on low temperatures, the initial peak needs to be as narrow as possible.

3.1.4 Temperature control

Our experimental area focuses on temperature dependent experiments in order to retrieve information about the hydrate shell, eutectic phase and interactions between lysozyme and the solute ^{23}Na and ^{35}Cl ions. Presence of a stable and wide range temperature control system is crucial. In figure 3.4 a rough demonstration of the cooling system is shown. A nitrogen dewar with a volume of about 15 l is filled with liquid nitrogen. The slowly evaporating, cool nitrogen gas is guided to the sample via a stainless steel pipe and double-walled quartz tubes. This gas can be heated while it passes the horizontal

²In frequency domain ppm (parts-per million) units are used. In NMR, ppm denotes the frequency deviation from a given central frequency in Hz divided by the central frequency value in MHz .

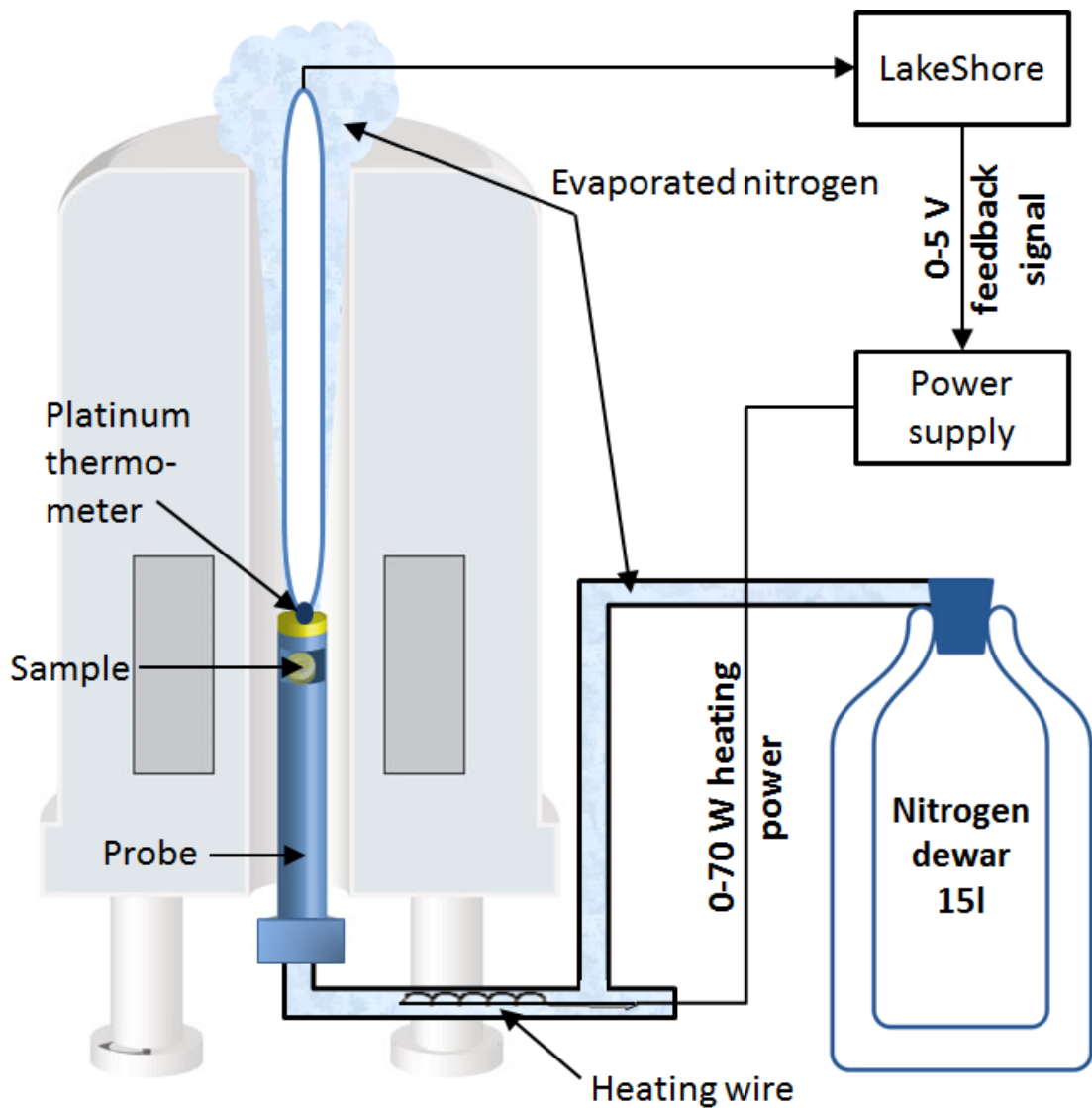


Figure 3.4: Temperature control system (source: [22])

section of the tubes using a 3Ω heating wire. The nitrogen gas of adjusted temperature will eventually cool or heat the sample (and the circuit as well). A platinum thermometer and the sample are placed less than 1 cm apart. The thermometer is attached to a Teflon rod as carrier and is hanged inside the magnet from above. It is attached to a *LakeShore 331 Temperature Controller* device via wires which run inside the Teflon. The LakeShore device is capable of temperature control using its built-in PID controls, but its output power is not sufficient for this arrangement. However, its output voltage can be used as feedback signal. This signal controls a power supply (capable of about 70 W output on the 3Ω heating wire) and thus regulates the temperature of the nitrogen gas heating and cooling the sample.

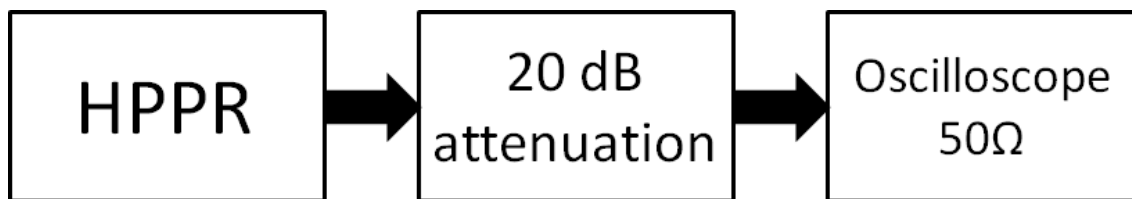


Figure 3.5: Experimental scheme for examination of output pulses (HPPR is the pre-amplifier of the NMR device.)

3.2 Spectrometer characterization

Usually, commercial spectrometers are considered to perform at the state of the art. However, we invested some efforts to understand the characteristics of our instrument and this thesis was performed on it for the first time after its installation. Detection of small signals is generally about maximizing SNR (signal-to-noise ratio), because the reason why a feeble signal is hard to detect is the possibility of it disappearing in the ambient noise. Since our experiments focus on the detection of low Larmor frequency nuclei, which therefore have low signals, it is important to thoroughly characterize the possible sources of noise and their contribution to the overall noise. This section demonstrates a way to characterize the NMR spectrometer properties. This study includes the examinations of pulses with respect to power and pulse width, as well as signal detection and noise figure characterization. Our set-up consists of a *Bruker Avance DRX 400* spectrometer equipped with a *Bruker Ultrashield 300* magnet. Signal acquisition and analysis is carried out using *TopSpin 1.3* and *OriginPro 8.5*. The presented protocol might as well serve as a future reference for inspecting the functionality of the spectrometer.

3.2.1 Output pulses

Output pulses were examined using the scheme in figure 3.5. The output is applied to an oscilloscope after a 20 dB attenuation (in order to secure the device) and a real time experiment is loaded. The aim is to observe the pulses appearing on the oscilloscope with respect to power and width. Figure 3.6 shows that pulse width is satisfyingly accurate as it was set to $25\ \mu\text{s}$ and the output pulse corresponds to that.

Power of pulses are set by a parameter named Square Power in the TopSpin 1.3 program. In order to determine the relation between this parameter and the actual output power, a series of real time experiments were performed using different Square Power values and measuring the peak-to-peak amplitudes of the output pulses on the scope.

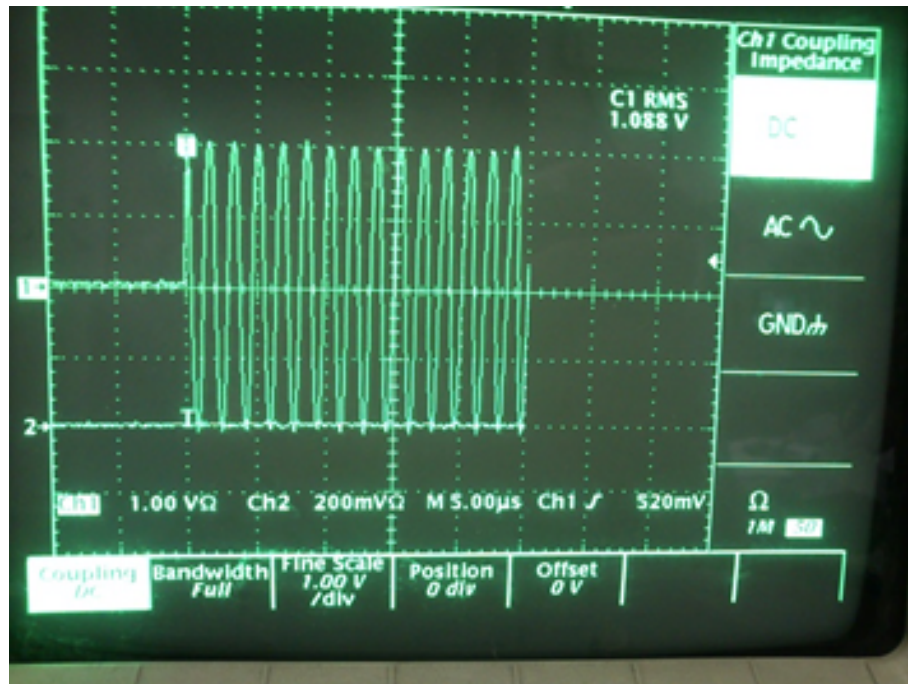


Figure 3.6: Photograph of an oscilloscope during a $25 \mu\text{s}$ pulse emission

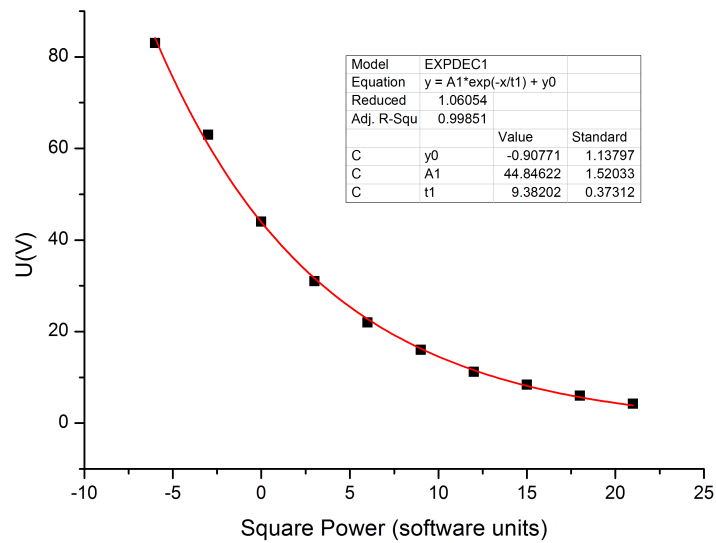


Figure 3.7: Peak-to-peak amplitude of pulses as a function of Square Power parameter

Taking into consideration the 20 dB attenuation, the output voltage as a function of Square Power (SP) is shown in figure 3.7 and is described by equation 3.1.

$$U_{amp} = 44.8V \cdot e^{-\frac{SP}{9.4}} \quad (3.1)$$

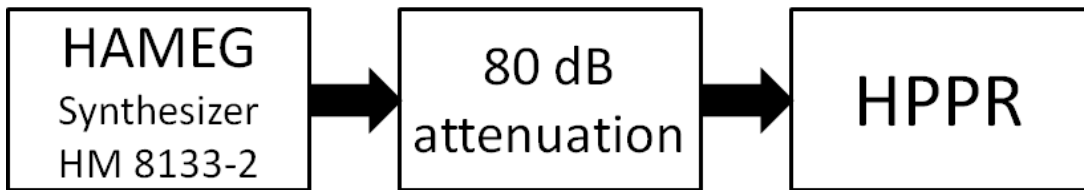


Figure 3.8: Experimental scheme for examination of signal detection

Expressing Square Power (SP) of this equation will result in equation 3.2. The conversion constant is approximately the usual 20 and negative because the program denotes the 100 W maximal power output as -6 dBm instead of 6 dBm . The actual maximum power measured on the scope is less than that (about 70 W) presumably due to the additional losses in the cables.

$$SP[\text{dBm}] = -21.46 \cdot \lg \frac{U_{amp}}{44.8V} \quad (3.2)$$

3.2.2 Signal detection

Input signals of known amplitude were examined with TopSpin 1.3 using the measurement scheme in figure 3.8. HPPR is the pre-amplifier of the NMR device. The aim was to determine the relation between the input signal amplitudes and the software units.

Using a -38 dBm input signal, the measured sine amplitude was observed in function of RG (Receiver Gain) and NS (Number of Scans). This confirmed that these parameters have a linear effect on the signal. Also, this experiment pointed out that the ADC saturates at around $3.5\text{ }\mu\text{V}$.

With this in mind, software units in function of input RMS (Root Mean Square) values were measured for both components of the quadrature detection and the magnitude of the signal as well. The results of this experiment are shown in figure 3.9. The experiments were performed with an NS value of 1 and the measured values were normalized by the receiver gain. Observation of real, imaginary and magnitude components resulted in the same values of software units, which assures reliability. The resulting curve is in fact linear through the origin. The relation between input voltage RMS and software units (S) is described by equation 3.3.

$$S = NS \cdot RG \cdot 0.006 \cdot U_{RMS}[\text{nV}] \quad (3.3)$$

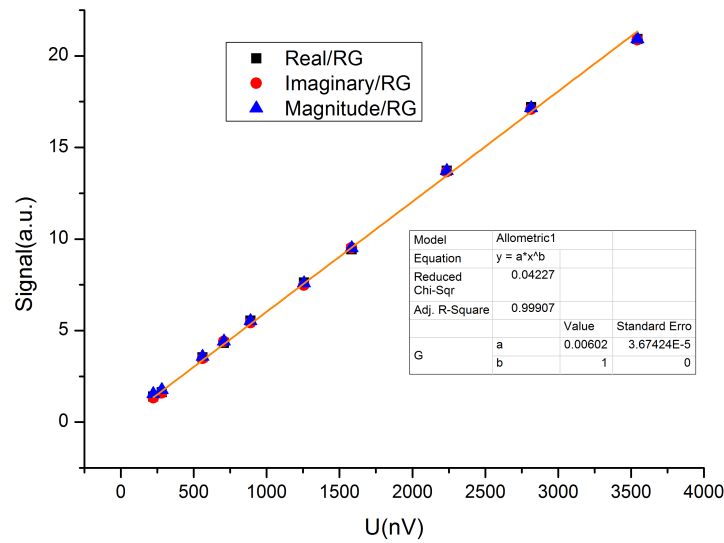


Figure 3.9: Software amplitude units as a function of input signal RMS value

3.2.3 Noise figure

The noise figure characterization was performed using the experimental scheme in figure 3.8. The -135 dBm input signal is very feeble so it disappears in the surrounding noise. The aim of this experiment was to examine the noise as a function of NS , RG and SWH (Spectrum Width in Hertz). A series of experiments were performed by altering one of these parameters while the other two were fixed. Noise values were taken as the standard deviation of the real and imaginary data.

Receiver Gain

The effect of increasing RG values on noise can be seen on figure 3.10. RG modifies the gain of the amplifier before the digitizer and after the low noise pre-amplifier situated in the HPPR. Therefore RG only effects the digit noise if any are present. The observed roughly linear increase of the noise as a function of RG therefore is in accordance with the expectations.

Number of Scans

The effect of increasing NS values on noise can be seen on figure 3.11. The fitted function confirms that this relation is in fact described by a square function as expected in case of Gaussian noise.

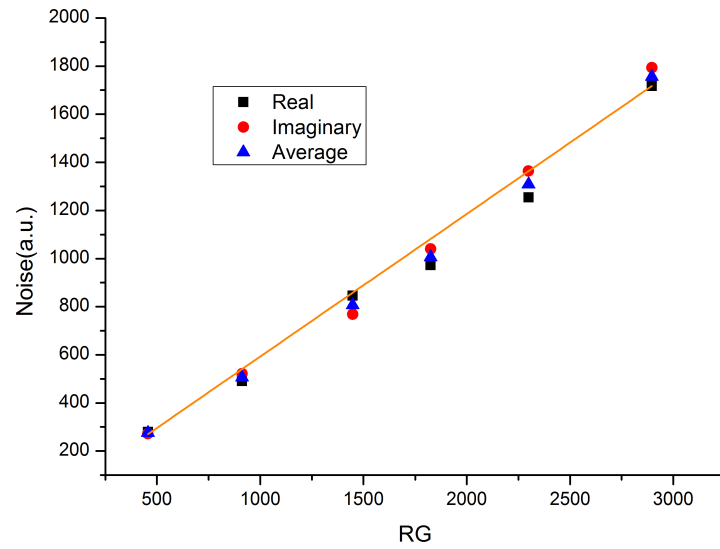


Figure 3.10: Noise level as a function of Receiver Gain. The solid curve is a fitted linear function.

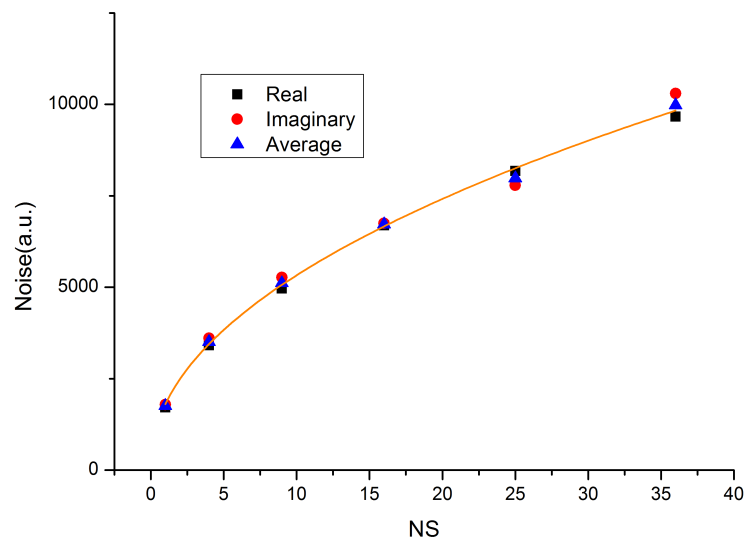


Figure 3.11: Noise level as a function of Number of Scans. The solid curve is a fitted function of \sqrt{NS} .

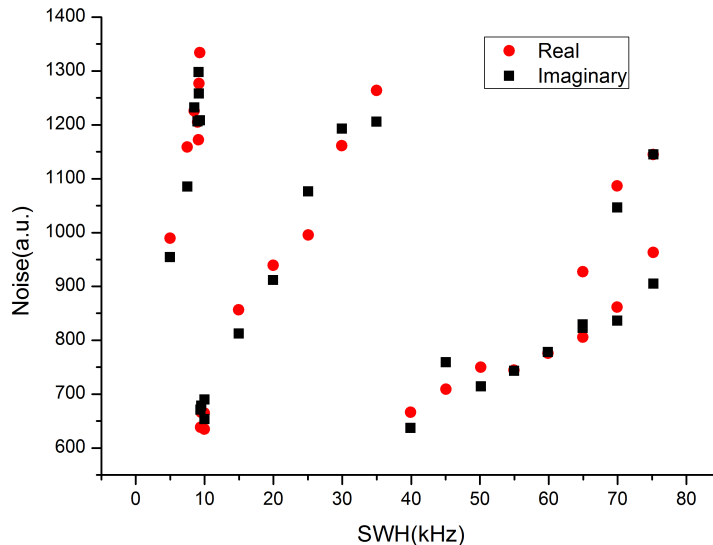


Figure 3.12: Noise level as a function of Spectral Width

Spectral Width

In a physical system, the minimal achievable noise level is limited by the Johnson-Nyquist noise [23, 24] described by equation 3.4, where N is the noise level, k_B is the universal Boltzmann constant, T is the temperature, R is the resistance of the system and BW is the band-width (in our case SWH stands for BW). This is a thermal limit caused by the thermal displacement of electrons in every non-zero temperature system.

$$N = \sqrt{4\pi \cdot k_B T \cdot R \cdot BW} \quad (3.4)$$

The effect of increasing SWH values on noise can be seen on figure 3.12. It is clear seen that SWH is not worth lowering below 45 kHz because that will not cause further decreasing in the absolute value of noise³. In addition, noise values normalized by \sqrt{SWH} are displayed on figure 3.13 which confirms that the noise of the spectrometer follows the characteristics of the Johnson-Nyquist noise. Calculation of this expected noise on room temperature and $50 \ \Omega$ resistance results in a similar value is taken to that of the measured. This assures that our spectrometer is operating at the lowest noise level that is physically possible.

³There is something unexplained in the operation of the spectrometer regarding the discontinuities of the function. However, displayed data contains the absolute noise values.

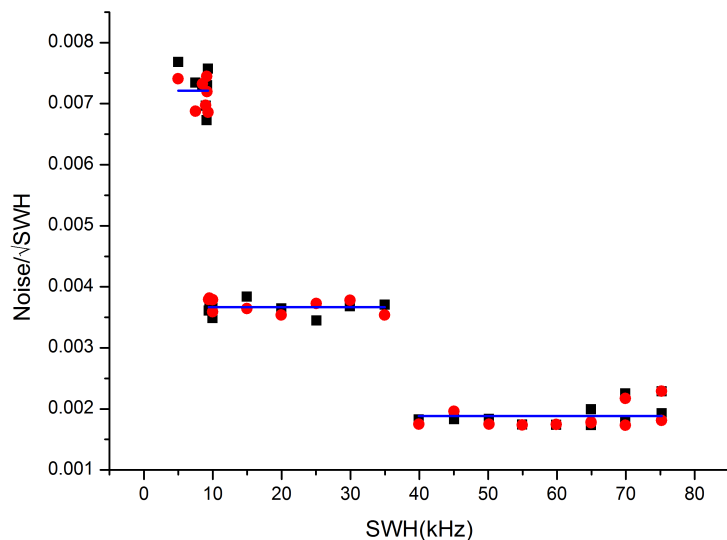


Figure 3.13: Normalized noise level as a function of Spectral Width

$$N = RG \cdot \sqrt{NS} \cdot 0.00189 \cdot \sqrt{SWH} \quad (3.5)$$

In conclusion, the spectrometer noise above 45 kHz band-width is described by equation 3.5.

3.3 Quantitative study of NMR experiments

NMR spectroscopy usually focuses on spectroscopic properties of the NMR lines and signal intensity is a rarely investigated parameter.

However, e.g. for calibration purposes and spectrometer characterization, it is required to perform quantitative NMR experiments. For instance, when signal intensity is correlated to instrumental parameters. To enable this I wrote an interactive *Matlab* interface and an underlying code that simulates an individual magnetic moment during a FID experiment. The simulation consists of two major parts. The actual codes are printed in appendix B.

3.3.1 Calculation of circuit parameters

The first part of the *Matlab* code focuses on signal transmission towards the receiver/transmitter coil given a certain parameter set concerning components of the circuit

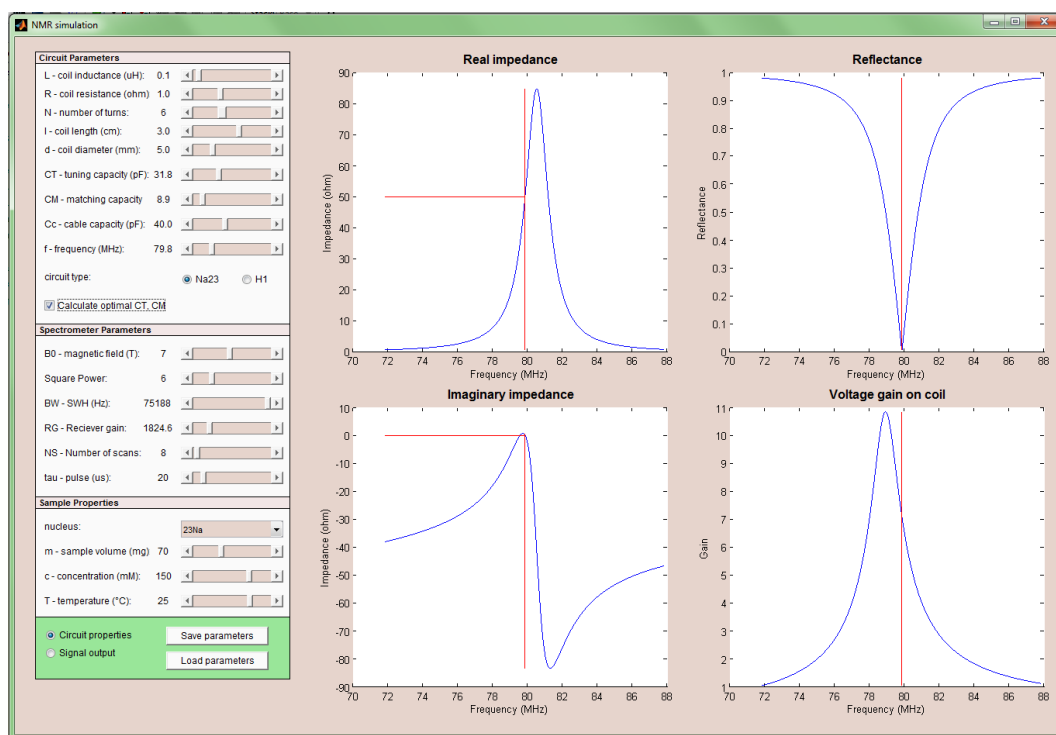


Figure 3.14: Interface design, circuit properties

(e.g. capacitances, inductance). On the interface, circuit properties are first set by the user (see figure 3.14). The following steps are necessary in order to determine the effectiveness of a given parameter set.

Transmittance between the spectrometer output and the probe

The necessity of a well-tuned circuit was explained in section 2.3.2. The code considers one of the probe circuits (see figure C.1) and calculates their net impedance at the given frequency. Then reflexion curve is calculated in the proximity of the given frequency as well as real and imaginary components of the net impedance (see figure 3.14). The program has a built-in option which calculates the ideal C_T and C_M parameters for a given parameter set according to the discussion in appendix C.

Voltage gain on the receiver/transmitter coil

In section 2.3.2, an advantage of using a complex electrical circuit was mentioned, namely that a voltage gain might appear on the receiver/transmitter coil. Voltage gain as a function of frequency about the central frequency is also calculated (see figure 3.14).

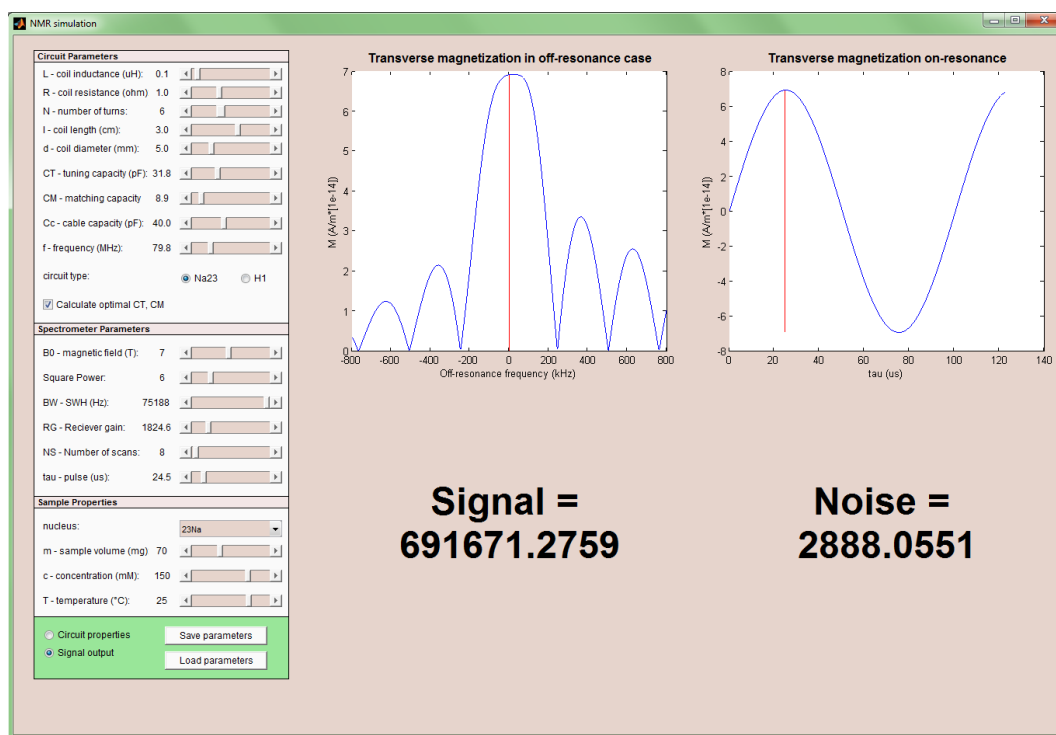


Figure 3.15: Bulk magnetization outputs

3.3.2 Calculation of bulk magnetization

Final output of the process is meant to be the initial signal amplitude appearing on the PC screen and an estimated noise value. In order to achieve that, first a couple of input parameters need to be given the user (e.g. TopSpin parameter values, sample properties; see figure 3.15). The steps of the calculation process are listed below.

- Given an SP value and the SP - *power* calibration function (see section 3.2.1), voltage applied to the probe is calculated.
- Using the voltage gain value calculated beforehand, voltage on the coil and consequently current in the coil are derived.
- A crude estimation of the induced B_1 magnetic field inside the coil is given by Ampère's circuital law.
- Given the properties of the detected nuclei and the sample, initial magnetization is obtained (using equation 2.24).
- Pulse width, B_1 and the aforementioned initial magnetization are, in our limit⁴, sufficient in order to calculate the x - y projection of the magnetization after the pulse.

⁴Assuming that pulses are relatively short compared to any of the relaxation times.

- Considering a precessing magnetization, voltage induced in the coil is derived using Faraday’s law of induction.

- Taking into consideration the energy transmission towards the output of the probe, the input signal of the spectrometer is obtained.

- Given the *input voltage - signal amplitude* (in TopSpin units) calibration function, the initial amplitude of the appearing signal is calculated.

Note that if either RG or NS values are larger than 1, it has to be taken into consideration using equation 3.3.

Noise estimation consists of three steps.

- Noise of the spectrometer is calculated using equation 3.5.

- Noise of the probe is approximated by the Johnson-Nyquist noise (see equation 3.4) of the coil.

- Assuming that both of the above noises are Gaussian, $\sigma_{net}^2 = \sigma_{spectrometer}^2 + \sigma_{probe}^2$ applies, where noise values are denoted by σ , thus an estimation of the overall noise can be calculated.

Setting *Signal output* as the interface mode, the estimated signal and noise values in TopSpin software units appear (see figure 3.15).

x - y projection of the initial magnetization after an off-resonance pulse is also calculated⁵ using the results of [14]. The magnetization value as a function of the extent of the off-resonance is shown (see figure 3.15). Rabi oscillation is demonstrated as the on-resonance magnetization value as a function of pulse width (τ).

Noise of the data measured on the sample of high concentration was evaluated as standard deviation of signal values fluctuating around zero. These were then normalized by RG and \sqrt{NS} resulting in values between 0.5 and 0.6. The corresponding noise level calculated by the program was 0.56 which assures the reliability of the noise calculation feature of the code. As for signal amplitude, measured values were within 10% of calculated values which also verifies that the code works correctly.

3.4 Preliminary experiments on saline solutions

Experiments on my part started with a series of preliminary measurements on saline solutions targeting the assessment of the limits and capabilities of the system I built. The experiments were performed on NaCl solutions of concentration 1.5 M⁽⁶⁾ and 150

⁵Transverse magnetization is in fact Fourier transform of a square pulse.

⁶1.5M = 1.5^{mol}/_l

mM using samples of mass between 50 mg and 80 mg . Temperature dependent T_1 , T_2 , $FWHM$ (Full Width at Half Maximum) and initial signal amplitude measurements were accomplished.

T_1 and T_2 measurements

For T_1 measurements Inversion Recovery NMR sequence was used (see section 2.1.3). Accumulated signals were considered using 8 different τ values. Signal processing and exponential fitting was carried out using TopSpin's built in T_1 processing tool.

T_2 measurements were performed using CPMG NMR sequence (see section 2.1.3). The first 6 consecutive echos were included in the analysis which was also carried out by TopSpin's built in routine for T_2 processing.

FWHM and signal amplitude measurements

Both $FWHM$ and signal amplitude were determined by an accumulated FID signal (see section 2.1.3). Using the NMR extension tool of OriginPro 8.5, a Lorentzian was fitted to the spectral data and two stretched exponential decays to the data in time domain.

As the initial relaxation takes place due to the magnetic field inhomogeneities rather than a real relaxation process (see section 2.1.3), the resulting function is neither strictly exponential in time domain nor strictly Lorentzian in frequency domain. However, both $FWHM$ and signal amplitude are of great importance as they refer to the internal inhomogeneities⁷ of the sample and the number of detected nuclei respectively. Thus an estimation of these parameters is necessary.

Error of fitting parameters of the Lorentzian represent the uncertainty of the peak. Therefore these values are always represented in the plotted curves. Relatively small values of deviations, especially on higher temperatures, feature the corresponding figures. Thus the estimated $FWHM$ values are considered satisfyingly accurate.

In case of signal amplitude, the main goal is to estimate the initial value as well as possible. Since the dead time of the measurements is relatively short (about 0.6 ms) compared to T_2^* (approximately 6 ms), a function fitting best to the beginning of the decay is considered suitable. This particular function happened to be the sum of two stretched exponential decays (see figure 3.16)⁸.

⁷Supposing that inhomogeneities present in B_0 remain constant, $FWHM$ trends are due to internal properties of the sample.

⁸Note that the evaluated initial signal amplitudes were also multiplied by their corresponding temperatures in order to compensate for the $\frac{1}{T}$ natural signal loss (see equation 2.24)

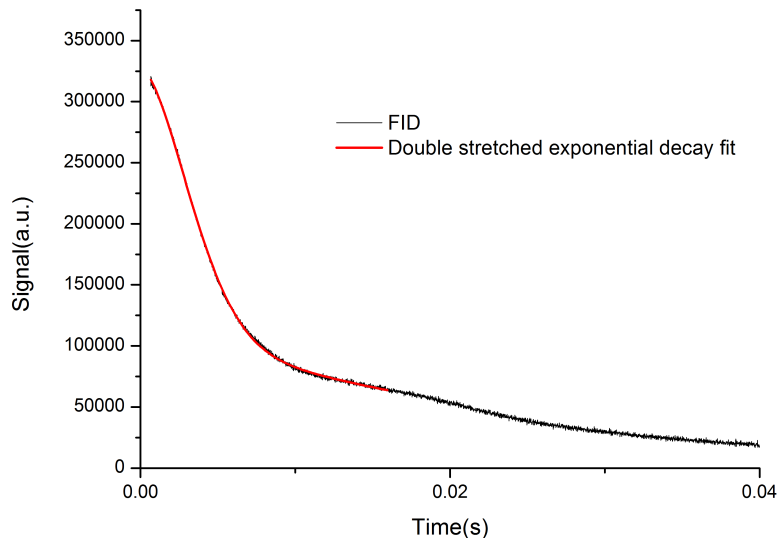


Figure 3.16: Fit of two stretched exponential decays to a FID

Protocol of temperature dependent experiments

First, the sample was slowly cooled down below a temperature where no signal was detected (e.g. 230 K). Then after at least 30 minutes, the sample was heated back up to room temperature. At each temperature where T_1 , T_2 , $FWHM$ or signal amplitude parameters were measured, time necessary for the measured temperature to reach the set temperature value and an additional 5 to 10 minutes was given the sample to achieve thermal equilibrium.

3.4.1 Analysis of T_1 and T_2 data

In section 2.2.1 equation 2.23 was deduced which describes the quadrupole relaxation of nuclei. The correlation time, τ_c , is usually assumed to have an Arrhenian dependence upon temperature [18] (see equation 3.6, where E is the activation energy of molecular motion). Furthermore, it was one of the first observations regarding relaxation rates that they conform approximately to the Arrhenius equation. Assuming the temperature dependence of the quadrupole coupling in equation 2.23 to be constant (at high temperatures), the aforementioned formula is indeed the temperature dependence of the correlation time.

$$\tau_c = \tau_\infty e^{\frac{E}{k_B T}} \quad (3.6)$$

However, the above principle only applies in case of highly diluted solutions. A solution of high concentration has higher viscosity in general which appears as a $\frac{\eta}{T}$ term in the relaxation rates and the correlation time with η being the viscosity [25]. A higher viscosity further increases the correlation time as it implies slower molecular motion.

According to various studies on the concentration dependence of viscosity [26, 27, 28], in case of a saline solution, viscosity varies between η_w and $1.4\eta_w$, where η_w is the viscosity of pure water.

3.4.2 Results and discussion

A series of measurements were performed on a sample of mass 73.6 mg and NaCl concentration of 1.5 M as well as a sample of mass 57.1 mg and concentration 150 mM . The following table shows the measured parameters in each case. Note that due to its lower Larmor frequency, reliable ^{35}Cl data could not be obtained in the low concentration case. However, it was still detectable. Also, in the case of ^{35}Cl , high concentration T_2 experiments were compromised by high signal deviations induced by low signals.

Concentration	Nucleus	T_1	T_2	FWHM	Signal amplitude
1.5 M	Na	✓	✓	✓	✓
1.5 M	Cl	✓		✓	✓
150 mM	Na	✓	✓	✓	✓
150 mM	Cl				

Relaxation times

Arrhenius plots of T_1 and T_2 data of both nuclei are shown in figures 3.17, 3.18 and 3.19. Melting points of the solutions considering their concentrations are denoted by dashed lines. It is clear that above the melting point, activation energies are close to the strength of the hydrogen bond in water which is around 0.24 eV [29]. In case of the lower concentration sample this value is slightly lower, but the order of magnitude is in accord with the concept. The fit is obviously not very reliable due to the fact that points were measured at only three temperature values.

Below the melting point, nuclei are still detectable (see next section). This is due to the fact that while crystallization of water molecules is in progress, water molecules in the proximity of the diluted ions remain motional thus providing a highly symmetrical environment and a narrow line. In fact, below the melting point corresponding to the initial concentration, diluted ions and water molecules in motion compose a solution of

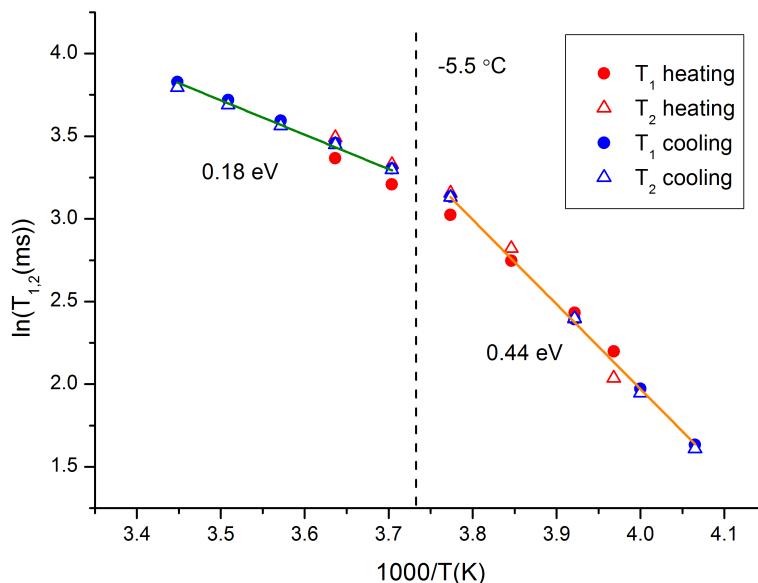


Figure 3.17: Arrhenius plot of T_1 and T_2 data measured on ^{23}Na (1.5 M sample)

concentration corresponding to the present temperature. After the concentration saturates (at around 6.18 M and $-21.2\text{ }^\circ\text{C}$), crystallization of the water molecules around the ions commence. This brings about the formation of a highly asymmetrical environment around the ions and a sudden line broadening (see section 2.2.1) as well as a drop in signal amplitude (see next section). The parameters of the saturation are called the eutectic temperature and the eutectic concentration.

Regarding the activation energy, below the melting point, it is supposed to be considerably higher than above the melting point because of the rise in concentration as well as viscosity (see section 3.4). In figures 3.17, 3.18 and 3.19, this effect undeniably appears. Also the elevated value of the activation energy is around 0.5 eV in all three cases.

Comparison of the measured relaxation times of ^{23}Na in the sample with concentration 150 mM are shown in figure 3.20. Data are in great accordance.

Signal amplitude and FWHM

Signal amplitude and $FWHM$ values are presented in figures 3.21, 3.22 and 3.23. Signal amplitude is constant above and abruptly drops below the eutectic temperature since at this point, environment of the diluted ions become highly asymmetrical (see previous section). The process occurring at the eutectic temperature is a first-order phase transi-

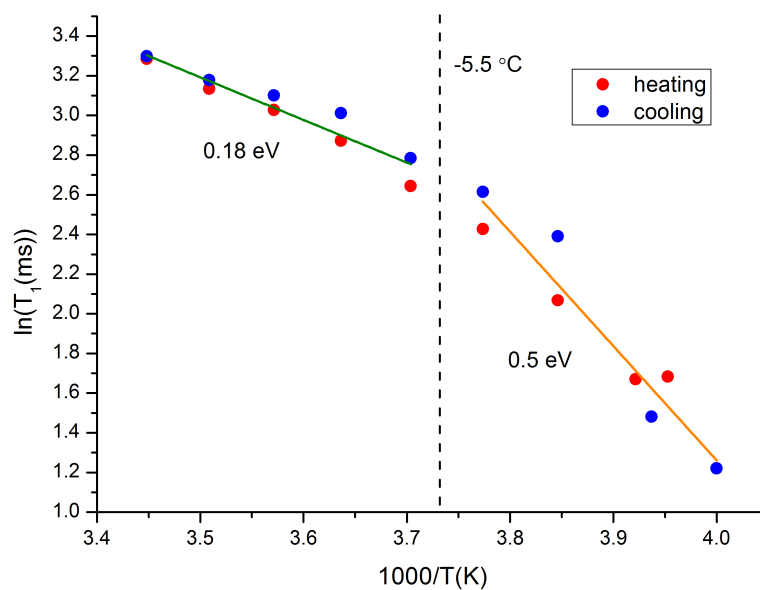


Figure 3.18: Arrhenius plot of T_1 data measured on ^{35}Cl (1.5 M sample)

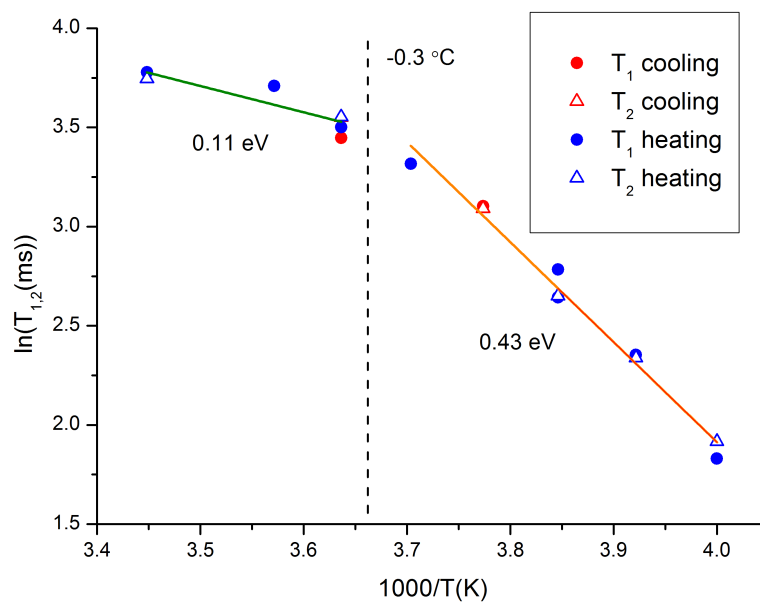


Figure 3.19: Arrhenius plot of T_1 and T_2 data measured on ^{23}Na (150 mM sample)

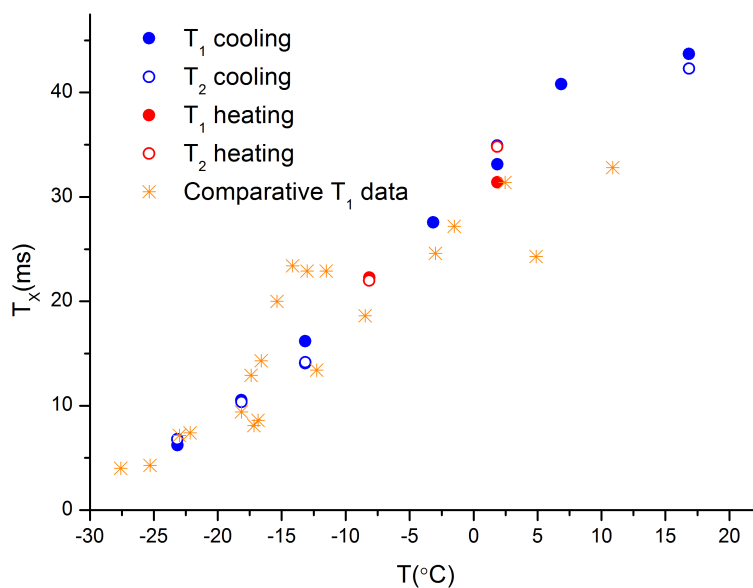


Figure 3.20: Comparison of relaxation time data with an unpublished study of Mónica Bokor

tion. Thus the hysteretic behavior of the $FWHM$, the sample is supercooled below the eutectic point. However, the endpoint of the hysteresis seems to coincide with the cutoff temperature of the signal amplitude. Though in the low concentration case, this exact temperature is hard to determine, in all three cases it appears to be around $-18\text{ }^{\circ}\text{C}$. This is about $3\text{ }^{\circ}\text{C}$ lower than the predicted value which might be due to a temperature gradient between the sample and the thermometer or a longer waiting time is needed before proceeding with the measurements at temperatures around the eutectic temperature.

Regarding signal amplitudes above the eutectic temperature, they differ greatly for the three cases. Comparison of the results is demonstrated in the following table. The normalized results are seemingly in great accordance.

Concentration (C)	Nucleus	Amplitude (S)	Larmor frequency (f_L)	Abundance (A)	Sample mass (m)	$\frac{S}{C \cdot f_L^2 \cdot A \cdot m}$
1.5 M	Na	11 000	79.35 MHz	1	73.6 mg	$1.6 \cdot 10^{-2}$
1.5 M	Cl	800	29.4 MHz	0.7553	73.6 mg	$1.1 \cdot 10^{-2}$
150 mM	Na	800	79.35 MHz	1	57.1 mg	$1.5 \cdot 10^{-2}$

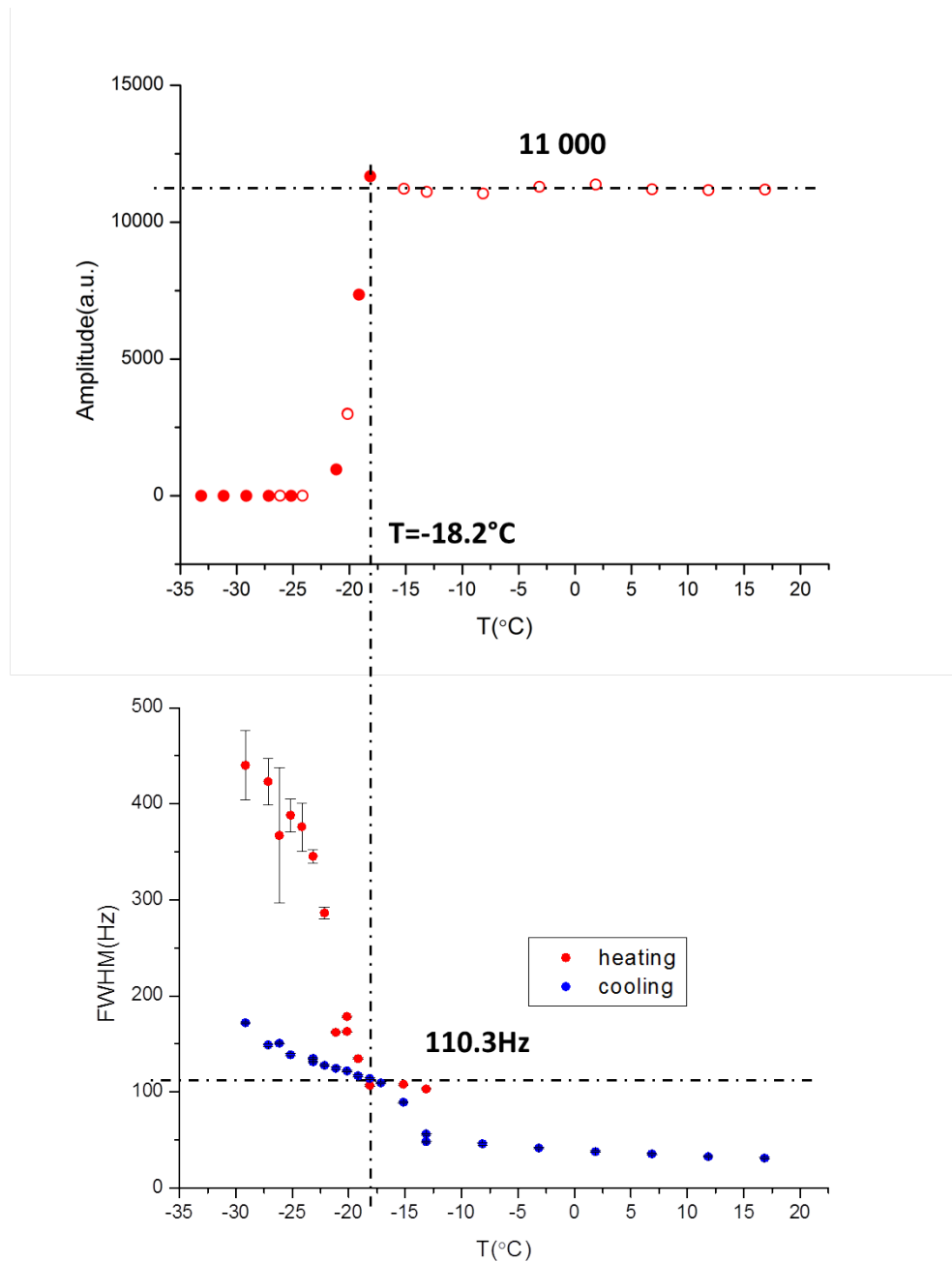


Figure 3.21: Signal amplitude and $FWHM$ data measured on ^{23}Na (1.5 M sample)

3.4.3 Conclusion

Preliminary experiments showed that the system produces satisfyingly accurate and reproducible data for ^{23}Na and ^{35}Cl measurements concerning T_1 , T_2 , $FWHM$ and signal amplitude. The results are in accordance with our predictions and previous studies.

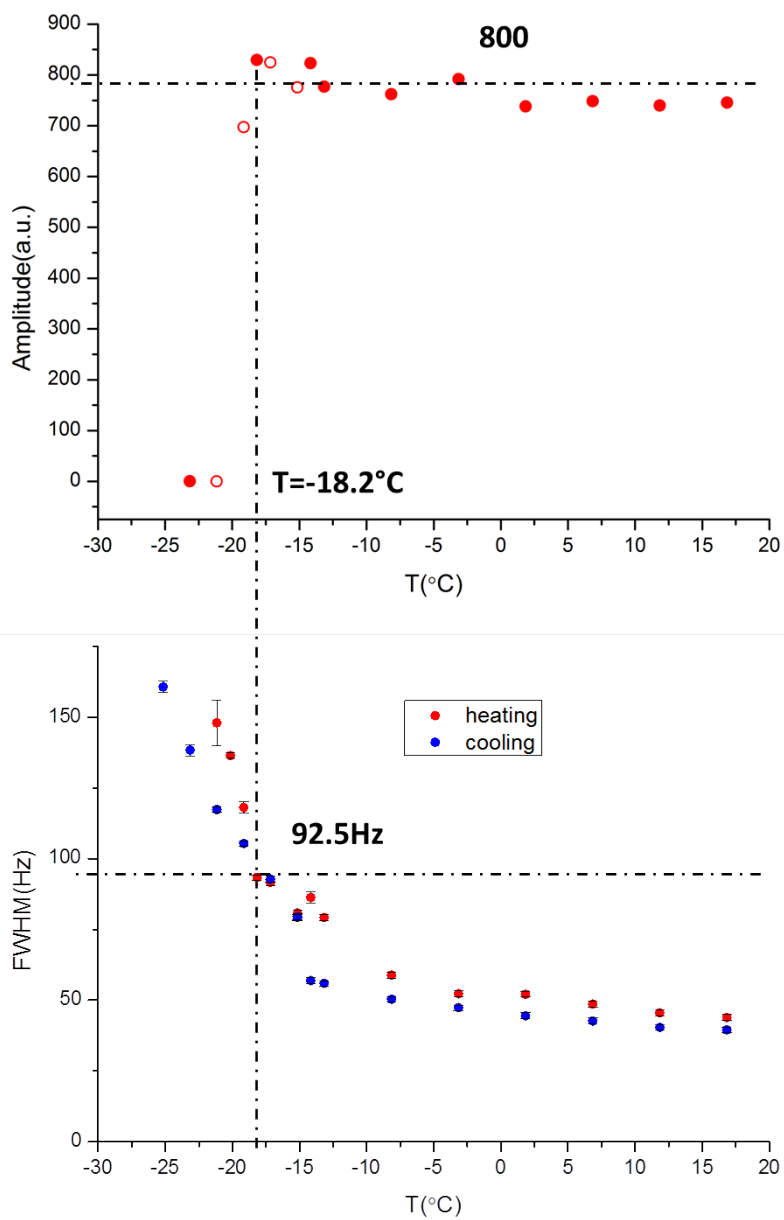


Figure 3.22: Signal amplitude and $FWHM$ data measured on ^{35}Cl ($1.5 M$ sample)

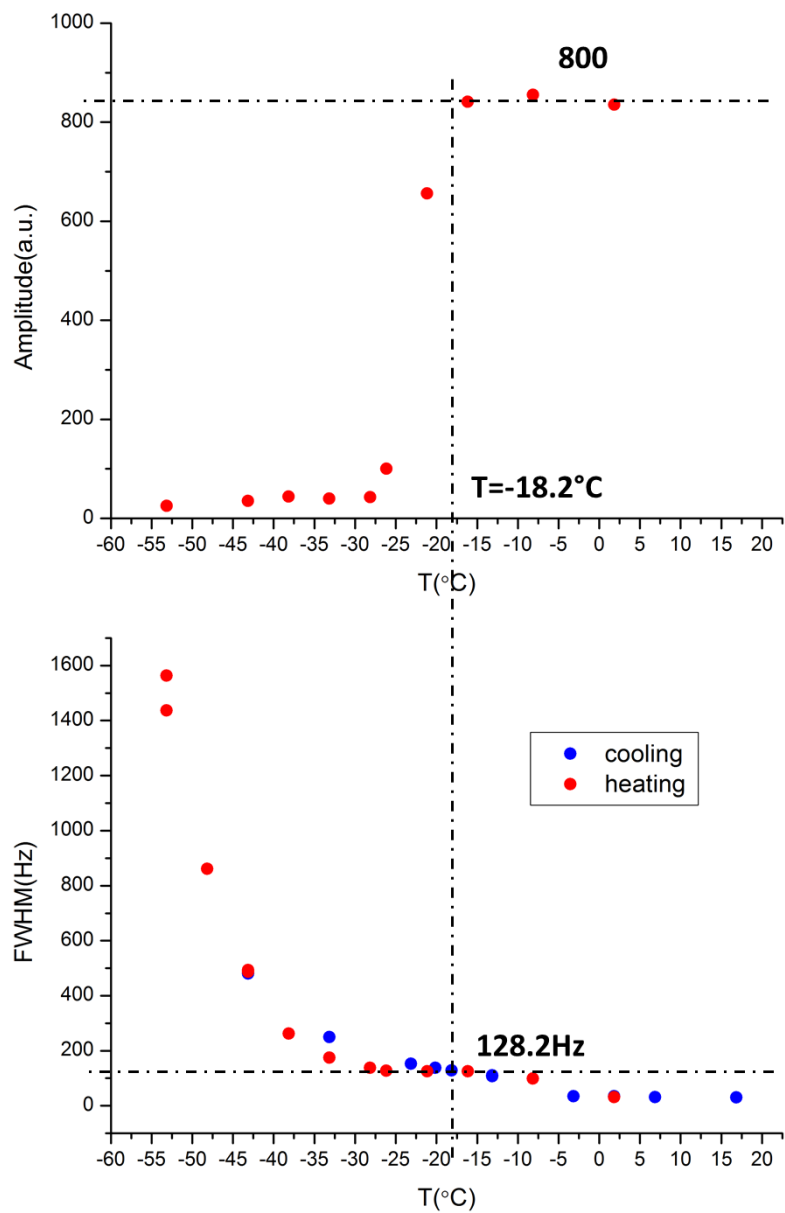


Figure 3.23: Signal amplitude and $FWHM$ data measured on ^{23}Na (150 mM sample)

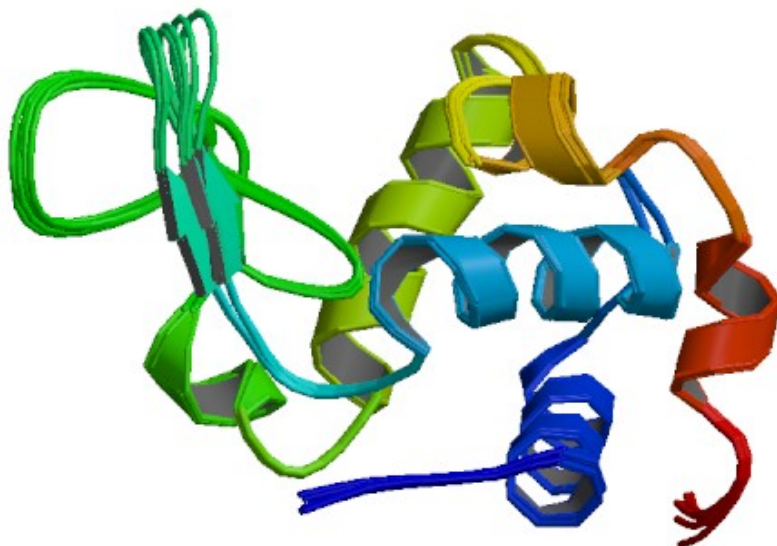


Figure 3.24: NMR solution structure of hen egg white lysozyme (Protein Data Bank id 1E8L). Protein chains are colored from the N-terminal to the C-terminal using a rainbow (spectral) color gradient. (source: [30])

Further improvements on the system aiming for evaluable ^{35}Cl data for samples of low concentration are possible and recommended.

3.5 Experiments on solutions with lysozyme

Lysozymes are enzymes that damage bacterial cell walls. It is abundant in various secretions such as saliva, tears and mucus. Lysozyme is one of the main proteins of egg white (see figure 3.24).

Experiments were also performed on a sample of concentration 150 mM with additional $50\frac{\text{mg}}{\text{ml}}$ lysozyme. The prepared sample was of mass 60.5 mg . Crystalline lysozyme from chicken egg white was purchased from Sigma (L6876-5G, protein content $> 90\%$) and was used without further purification.

In figure 3.25, the measured signal amplitude and FWHM values are presented. One of the prominent characteristics of the measured curves is that detectable signal appears around $-60\text{ }^{\circ}\text{C}$ instead of $-20\text{ }^{\circ}\text{C}$. This is probably caused by the large protein surface which unables water molecules to crystallize in their proximity. Thus the ^{23}Na nuclei connected to the surface are still in a liquid environment even significantly below the eutectic temperature. The presence of water molecules in motion is also ascertained by the work of Tamás Verebélyi who performed ^1H NMR experiments on 100 mM saline solutions containing $50\text{ }\frac{\text{mg}}{\text{ml}}$ lysozyme-solution. In figure 3.26, appearance of motional water is evident at around $-45\text{ }^{\circ}\text{C}$.

The other interesting feature of the signal amplitude curve is the rapid drop in signal intensity around the eutectic point. This fact might lead to the conclusion that besides near protein surfaces, ^{23}Na nuclei are also present in pure (bulk) water environments. This result is in accordance with DSC (Differential Scanning Calorimetry) measurements of Pawel Kamasa (see figure 3.27). Around the eutectic temperature, a phase transition occurs in the sample which is indicated by the endothermal peak appearing in the plot. A peak is still present in the lysozyme added case, however its integral is smaller. Therefore a part of the ^{23}Na nuclei still participates in the phase transition, referring to their not protein-bound state.

Other peculiar features of the measured curves are yet to be explained in detail.

It is also worth mentioning that even if ^{35}Cl signals were not evaluable, chlorine nuclei were still detectable. However, unlike sodium, chlorine became undetectable below approximately $-23\text{ }^{\circ}\text{C}$.

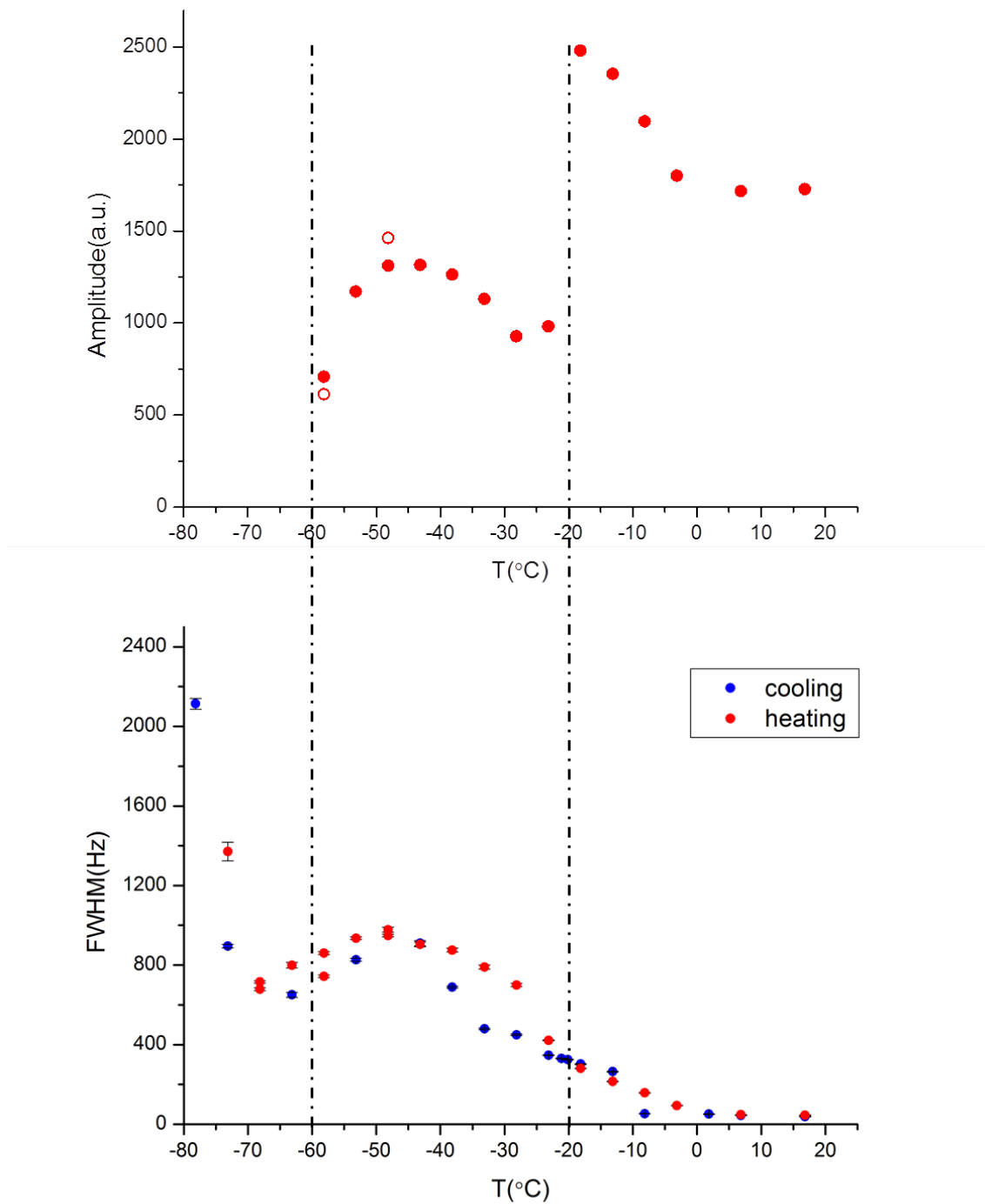


Figure 3.25: Signal amplitude and $FWHM$ data measured on ^{23}Na (150 mM sample with lysozyme addition)

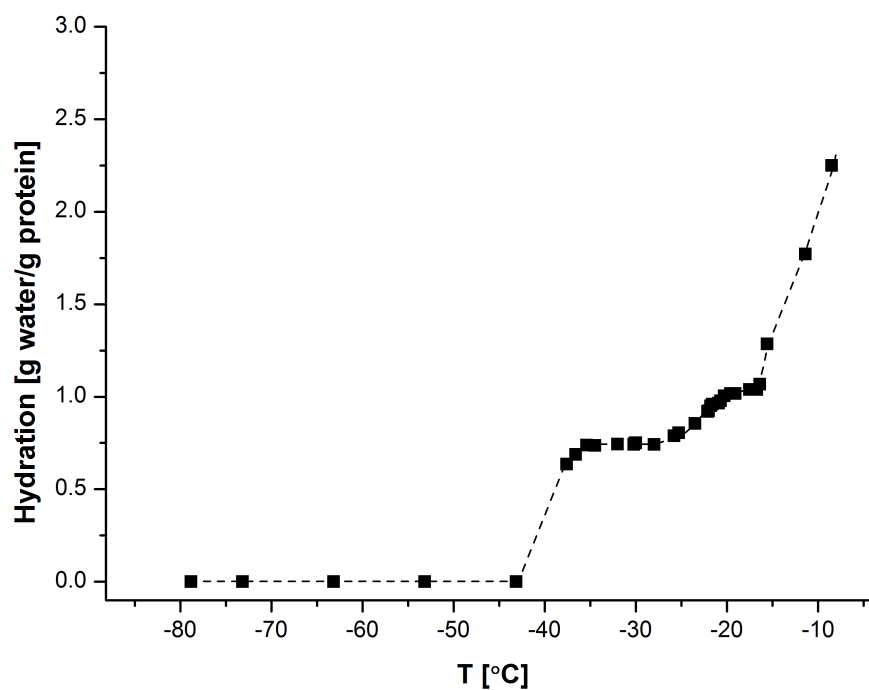


Figure 3.26: Signal amplitude data measured on ^1H (aqueous solution of 100 mM NaCl and $50\frac{\text{mg}}{\text{ml}}$ lysozyme) by Tamás Verebélyi

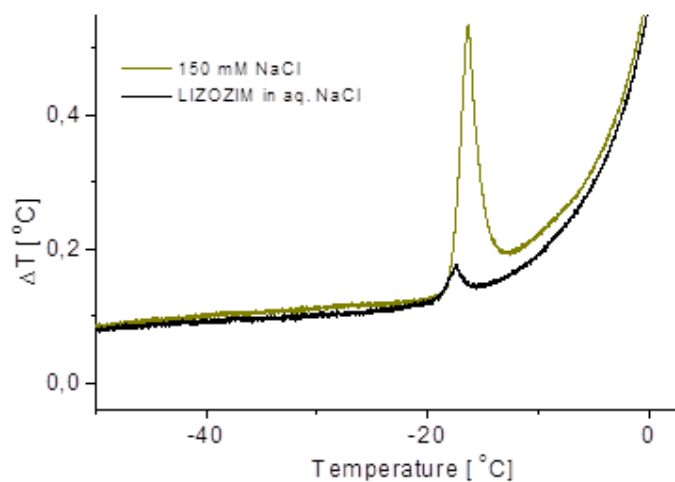


Figure 3.27: DSC measurements on 150 mM saline sample with and without lysozyme addition ($50\frac{\text{mg}}{\text{ml}}$) by Pawel Kamasa

Chapter 4

Summary and conclusions

Characterization of molecular dynamics in saline solutions is crucial while aiming for a thorough understanding of the properties and mechanisms of extra- and intracellular fluids in the human body. My thesis focuses on NMR detection of ^{23}Na and ^{35}Cl nuclei in saline solutions of concentration close to that of the human body. It includes a thorough study of NMR probes as well as the development of a high sensitivity probe, assemblage of a temperature control system, characterization of the spectrometer and preliminary experiments on saline solutions of high and low concentrations in order to assess the effectiveness of the system.

^{23}Na and ^{35}Cl nuclei are typically hard to detect due to their low Larmor frequencies. A low concentration of said nuclei in our sample further aggravates the problem. Moreover, a high noise level causes low signals to become generally undetectable. I developed a high sensitivity probe by maximizing the filling factor and ensuring that it is tunable to the Larmor frequencies of both nuclei, thus enabling high energy transmission between the spectrometer and the probe. Also, I thoroughly characterized the spectrometer, confirming that it operates at the lowest noise level which is physically possible. Therefore every condition was given to detect low signals.

In the determination of molecular properties of saline solutions, temperature dependent experiments provide an informative perspective. Consequently, a stable temperature control system is crucial. Such a system was developed and deemed well functioning for our experiments between $-80\text{ }^{\circ}\text{C}$ and room temperature.

Preliminary experiments performed on saline solutions of concentrations 1.5 M and 150 mM proved the set-up to be operating well. On ^{23}Na , generally known molecular features were observable with the results being in accordance with previous studies. Due to its lower Larmor frequency, signals measured on ^{35}Cl were not evaluable in the lower

concentration case, however, it remained detectable. I propose a continuation of set-up optimization for low signals targeting the solution of the problem of unevaluable ^{35}Cl signals.

As a demonstration of the potential of the developed system, temperature dependent experiments were performed on a solution of *150 mM* NaCl and *50 mg/ml* lysozyme. The measured data confirmed properties of the solution which were observed previously as well as other features that are yet to be examined in detail.

Long term purpose of this study is examination of molecular properties of protein added saline solutions which approximate the composition of fluids in the human body. I declare the assembled measurement system to be suitable for this objective.

Appendix A

The effect of a stationary water dipole on a quadrupole nucleus

In this section a crude estimation of line broadening due to quadrupole interaction is discussed. Let us consider a water dipole near a quadrupole nucleus. Electrostatic potential produced by the dipole is expressed by equation A.1, where p denotes the electric dipole moment of a water molecule and ϵ_0 is the vacuum permittivity. ϑ' , ϑ , Θ and r are explained in figure A.1. According to equation 2.23 in section 2.2.1, second partial derivative along z axis of the aforementioned potential needs to be calculated. Note that the coordinate system must coincide with the principal axis system of the nucleus (see figure A.1). In this estimation, it is assumed that the axis of the dipole is radial to the position of the nucleus (see figure A.1).

$$V(r, \vartheta, \phi) = \frac{1}{4\pi\epsilon_0} \frac{p \cdot \sin\vartheta'}{r^2} = \frac{1}{4\pi\epsilon_0} \frac{p \cdot \sin(\vartheta - \Theta)}{r^2} \quad (\text{A.1})$$

In order to prepare the second partial derivative, electrostatic potential has to be expressed in Cartesian coordinates (see equation A.2).

$$V(x, y, z) = \frac{1}{4\pi\epsilon_0} \frac{p}{r^2} \left\{ \cos\Theta \frac{x}{r} - \sin\Theta \frac{z}{r} \right\} = \frac{p}{4\pi\epsilon_0} \frac{x \cdot \cos\Theta - z \cdot \sin\Theta}{(x^2 + z^2)^{3/2}} \quad (\text{A.2})$$

First and second partial derivatives of the potential with respect to z are given by equation A.3 and A.4

$$\partial_z V = \frac{p}{4\pi\epsilon_0} \frac{2z^2 \cdot \sin\Theta - 3xz \cdot \cos\Theta - x^2 \cdot \sin\Theta}{(x^2 + z^2)^{5/2}} \quad (\text{A.3})$$

$$\partial_z^2 V = \frac{p}{4\pi\epsilon_0} \frac{-6z^3 \cdot \sin\Theta + 12z^2 x \cdot \cos\Theta - zx^2 \cdot \sin\Theta - 3x^3 \cdot \cos\Theta}{(x^2 + z^2)^{7/2}} \quad (\text{A.4})$$

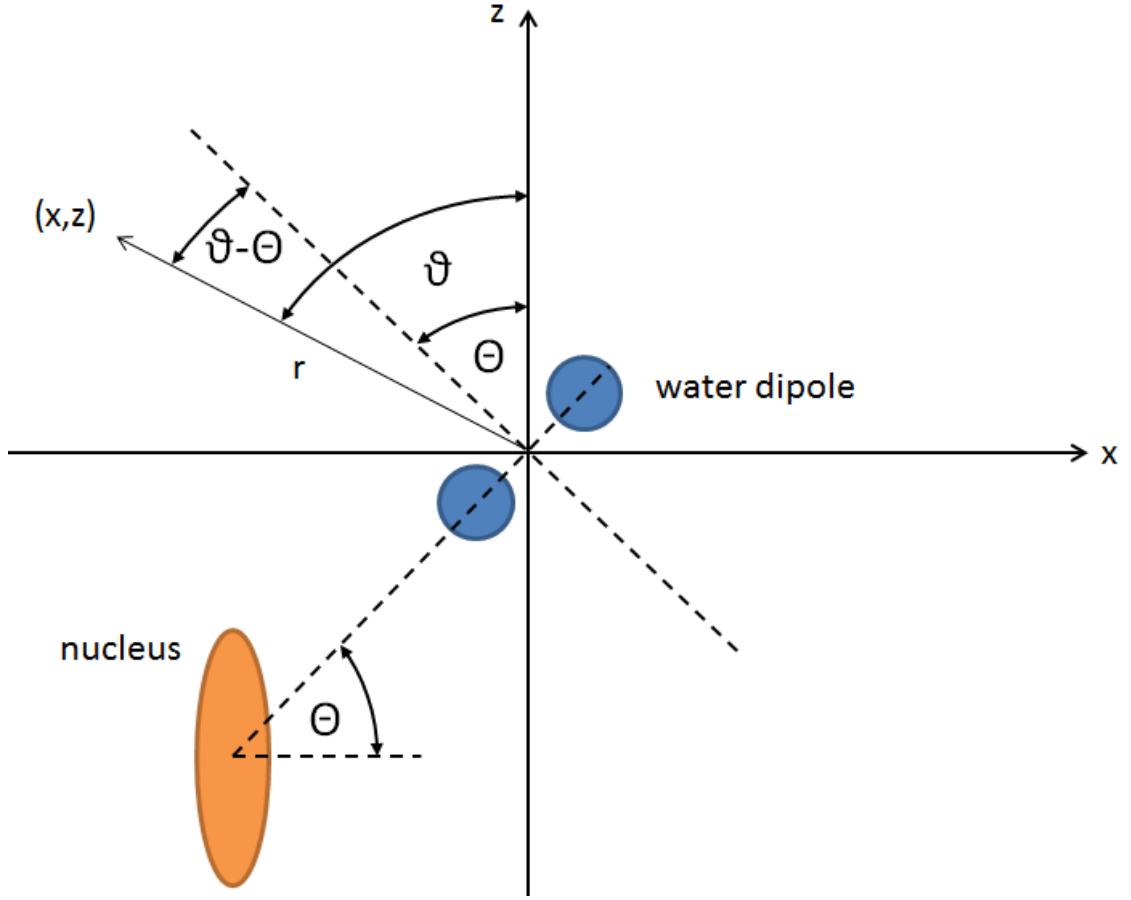


Figure A.1: Configuration of a water dipole around a quadrupole nucleus

At this point, returning to polar representation is beneficial, as it leads to a more compact expression (see equation A.5).

$$\begin{aligned} \partial_z^2 V(r, \vartheta, \phi) = & \frac{1}{4\pi\epsilon_0} \frac{p}{r^4} (-6\cos^3\vartheta \cdot \sin\Theta + 12\cos^2\vartheta \sin\vartheta \cdot \cos\Theta - \\ & - \cos\vartheta \sin^2\vartheta \cdot \sin\Theta - 3\sin^3\vartheta \cdot \cos\Theta) \end{aligned} \quad (\text{A.5})$$

Assuming that our nucleus is at coordinates $(r, \pi - \Theta, \phi)$, the expression is further simplified (see equations A.6 and A.7).

$$\begin{aligned} \partial_z^2 V(nucleus) = & \frac{1}{4\pi\epsilon_0} \frac{p}{r^4} (6\cos^3\Theta \cdot \sin\Theta + 12\cos^3\Theta \sin\Theta + \\ & + \cos\Theta \sin^3\Theta - 3\sin^3\Theta \cdot \cos\Theta) \end{aligned} \quad (\text{A.6})$$

$$\partial_z^2 V(nucleus) = \frac{1}{4\pi\epsilon_0} \frac{p}{r^4} \cdot 2\cos\Theta \sin\Theta \cdot (9 - 11\sin^2\Theta) = \frac{1}{4\pi\epsilon_0} \frac{p}{r^4} \cdot h(\Theta) \quad (\text{A.7})$$

The last part of equation A.7 is basically a general form of $\partial_z^2 V$, since in every possible configuration of the nucleus and the dipole, an extra r^2 will appear in the denominator (due to the derivation) and the expression will be further multiplied by a function that is representative of the configuration. The question is, what possible values this function may take. In this approximation of the problem, the resulting function takes values between -5.4518 and 5.4518 (see equation A.8).

$$0 \leq |h(\Theta)| \leq 5.4518 \quad (\text{A.8})$$

After substituting $\partial_z^2 V$ into equation 2.23 in section 2.2.1, the following expression is obtained. The results were calculated using values $Q = 10 \text{ fm}^2$, $r = 0.1 \text{ nm}$, $p = 6 \cdot 10^{-30} \text{ Cm}$ and $\tau_c = 1 \text{ ps}$. Note that this crude estimation shows, that only the dipoles in the close proximity of the nucleus have considerable effect on spectrum widening, since $\Delta f \propto \frac{1}{r^8}$.

$$\begin{aligned} \Delta f &= \frac{2\pi}{5} \left(\frac{eQ}{h} \frac{1}{4\pi\epsilon_0} \frac{p}{r^4} \right)^2 \tau_c \cdot \left(\sum_{dipole} h(\Theta) \right)^2 \\ &\approx 1\text{Hz} \cdot \left(\sum_{dipole} h(\Theta) \right)^2 \end{aligned} \quad (\text{A.9})$$

Equation A.9 shows that given a few water dipoles with accumulating potential at the position of the nucleus, spectral line can be as wide as a few 10 times greater than the initial value. Note that line-width is in general supposed to refer to the so-called *nuclear shielding* effect [19]. Electron shells of the quadrupole nucleus suffer deformation. This deformity induces a non-zero V_{zz} in the position of the nucleus. This effect however appears in case of both symmetrical and asymmetrical environments resulting in a general line broadening regardless of the configuration of water dipoles.

Appendix B

Matlab code of signal and noise calculations

```
function [CT,CM]=ak_CalcCTCM(L,R,Cc,CircType,Freq)

w=2*pi*Freq;

switch CircType
    case 'Na23'
        b=50^2*w*Cc/(1+50^2*w^2*Cc^2);
        a=sqrt(b*(1-w*Cc*b)/w/Cc);
        CT=(L-sqrt(R/a*L^2+R^2/w^2*R/a-R^2/w^2))/(w^2*L^2+R^2);
        CM=1/w*((1+(w^2*CT*L)^2+w^2*CT^2*R^2)-(2*w^2*CT*L))/((w*CT*R^2+w*L+2*b*w^2*CT*L)...
            -(w^2*CT*L*w*L+b+b*(w^2*CT*L)^2+b*w^2*CT^2*R^2));
    case 'H1'
        CM=1/(w*(w*L-sqrt(50*R-R^2)));
        CT=(w^2*L*CM-1)/(CM*w^2*(R^2+(w*L-1/w/CM)^2))-Cc;
end

CM=round(1e13*CM)/1e13;
CT=round(1e13*CT)/1e13;

end
```

```

function ak_CalcBulkMagnetization(L,R,C1,C2,Cc,Turn,CoilLen,CoilDia,MagnField,gamma,...
    Vol, Conc, abundance,spin,Temp,CircType,Freq,FreqMin,FreqMax, Pow, BW, RG, NS,...
    tau, ak_Axes1, ak_Axes2, ak_Title1, ak_Title2, ak_Title3, ak_Title4)

Freq_vec=linspace(FreqMin, FreqMax, 500);
gamma=gamma*1e6;

%% calculate total impedance and voltage gain
switch CircType
case 'Na23'
    Z_vec=1./(1i*2*pi*Freq_vec*Cc+1./(1./(1i*2*pi*Freq_vec*C2)+1./(1i*2*pi*Freq_vec*C1+...
        1./(1i*2*pi*Freq_vec*L+R))));
    ImpedanceGain=(1./(1i*2*pi*Freq_vec*C1+1./(1i*2*pi*Freq_vec*L+R)))/...
        (1./(1i*2*pi*Freq_vec*C1+1./(1i*2*pi*Freq_vec*L+R))+1./(1i*2*pi*Freq_vec*C2));
case 'H1'
    Z_vec=1./(1i*2*pi*Freq_vec*(Cc+C1)+1./(1./(1i*2*pi*Freq_vec)+1i*2*pi*Freq_vec*L+R));
    ImpedanceGain=(1i*2*pi*Freq_vec*L+R)/(1i*2*pi*Freq_vec*L+R-1i./(2*pi*Freq_vec*C2));
end

%% Induced Magnetic Field
Refl=abs(Z_vec-50*ones(length(Z_vec),1)))/abs(Z_vec+50*ones(length(Z_vec),1)); %reflectance

IncidentVoltage=44.8*exp(-Pow/9.4); %maximum voltage according to conversion

TransmittedVoltage=(1+Refl)*IncidentVoltage; %transmitted voltage

CoilCurrent=abs((TransmittedVoltage.*ImpedanceGain)/(1i*2*pi*Freq_vec*L+R)); %current on coil

InducedMagnField=4*pi*1e-7*Turn*CoilCurrent/CoilLen; %magnetic field in coil

%% Initial Magnetization
NumberOfNuclei=ak_NumberOfNuclei(Vol, Conc, abundance);

M0=(2*pi*gamma)^2*(6.34e-34)^2*MagnField*NumberOfNuclei*spin*(spin+1)/3/(1.381e-23)/Temp;
%incident magnetization (total)

%% calculation of off-resonance behaviour

dw_vec=Freq-Freq_vec;
wl_vec=gamma*2*pi*InducedMagnField;
theta=atan(wl_vec./dw_vec);
weff=sqrt(dw_vec.^2+wl_vec.^2);

Mx=M0*sin(theta).*cos(theta).(1-cos(weff*tau));
My=M0*sin(theta).*sin(weff*tau);

M=sqrt(Mx.^2+My.^2);

% %Mx,My - dw
%
% plot(dw_vec*1e-3, Mx*1e24, 'Parent', ak_Axes3);
% set(ak_Title3, 'String', 'Transverse magnetization (x axis)');
% xlabel(ak_Axes3,'Off-resonance frequency (kHz)');
% ylabel(ak_Axes3,'Mx (A/m*[1e-24])');
%
% if and(FreqMin<Freq, FreqMax>Freq)
%     line([0 0],[min(Mx*1e24) max(Mx*1e24)],'Color','r','Parent',ak_Axes3);
% end
%

```

```

% plot(dw_vec*1e-3, My*1e24, 'Parent', ak_Axes4);
% set(ak_Title4, 'String', 'Transverse magnetization (y axis)');
% xlabel(ak_Axes4, 'Off-resonance frequency (kHz)');
% ylabel(ak_Axes4, 'My (A/m*[1e-24])');
%
% if and(FreqMin<Freq, FreqMax>Freq)
%     line([0 0],[min(My*1e24) max(My*1e24)], 'Color', 'r', 'Parent', ak_Axes4);
% end

plot(dw_vec*1e-3, M*1e14, 'Parent', ak_Axes1);
set(ak_Title1, 'String', 'Transverse magnetization in off-resonance case');
xlabel(ak_Axes1, 'Off-resonance frequency (kHz)');
ylabel(ak_Axes1, 'M (A/m*[1e-14])');

if and(FreqMin<Freq, FreqMax>Freq)
    line([0 0],[min(M*1e14) max(M*1e14)], 'Color', 'r', 'Parent', ak_Axes1);
end

%% tau dependence of transverse magnetization (on-resonance)

InducedMagnField=InducedMagnField(length(InducedMagnField)/2);

wl=gamma*2*pi*InducedMagnField;
tau_vec=linspace(0, 5*tau, 500);

M=M0*sin(wl*tau_vec);

%M - tau

plot(tau_vec*1e6, M*1e14, 'Parent', ak_Axes2);
set(ak_Title2, 'String', 'Transverse magnetization on-resonance');
xlabel(ak_Axes2, 'tau (us)');
ylabel(ak_Axes2, 'M (A/m*[1e-14])');

line([tau*1e6 tau*1e6],[min(M*1e14) max(M*1e14)], 'Color', 'r', 'Parent', ak_Axes2);

%% induced voltage on coil and output

M=M0*sin(wl*tau);
%InducedVoltage=2*pi*Freq*M*4*pi*1e-7*Turn/CoilLen; %amplitude

InducedVoltage=2*pi*Freq*M/2*sqrt(4*pi*1e-7*L/CoilLen/(CoilDia^2/4*pi)); %amplitude [V]

%output voltage

switch CircType
case 'Na23'
    OutputVoltage=InducedVoltage.*(1./(1/50+1i*2*pi*Freq*Cc))./...
        (1./(1/50+1i*2*pi*Freq*Cc)+1./(1i*2*pi*Freq*C2));
case 'H1'
    OutputVoltage=InducedVoltage.*abs(1./(1/50+1i*2*pi*Freq*(C1+Cc)))./...
        (1./(1/50+1i*2*pi*Freq*(C1+Cc))+1./(1i*2*pi*Freq*C2));
end

OutputVoltage=abs(OutputVoltage);

Signal=RG*NS*(0.006*OutputVoltage*1e9);

NoiseOfSpectrometer=0.00189*sqrt(BW);

```

```
NoiseOfCircuit=sqrt(4*1.381e-23*Temp*BW*R)*1e9; %nV
NoiseOfCircSU=0.006*NoiseOfCircuit;

Noise=sqrt(NoiseOfSpectrometer^2+NoiseOfCircSU^2)*RG*sqrt(NS);

set(ak_Title3, 'String', ['Signal = ' num2str(Signal)]);

set(ak_Title4, 'String', ['Noise = ' num2str(Noise)]);
```

Appendix C

Optimization of C_T and C_M

This section is dedicated to demonstrate the mathematics behind optimization of an NMR circuit with respect to energy transmission. The aim is to deduce an expression describing C_T and C_M for a given L , R and ω_L (inductance and resistance of the receiver coil and angular frequency respectively)¹. The circuits described in section 2.3.2 are completed with another capacitance. This refers to the fact that a probe is of a given size and the signal has to be transmitted from the top to the bottom of it, usually via a semi-rigid cable, which represents an imprescindible capacitance between the circuit and the output of the probe (see figure C.1). This extra capacitance is denoted by C_C . Effective transmission

¹ ω_L is the angular Larmor frequency of the observed nucleus. Parameters of the receiver/transmitter coil are mostly dependent on sample dimensions.

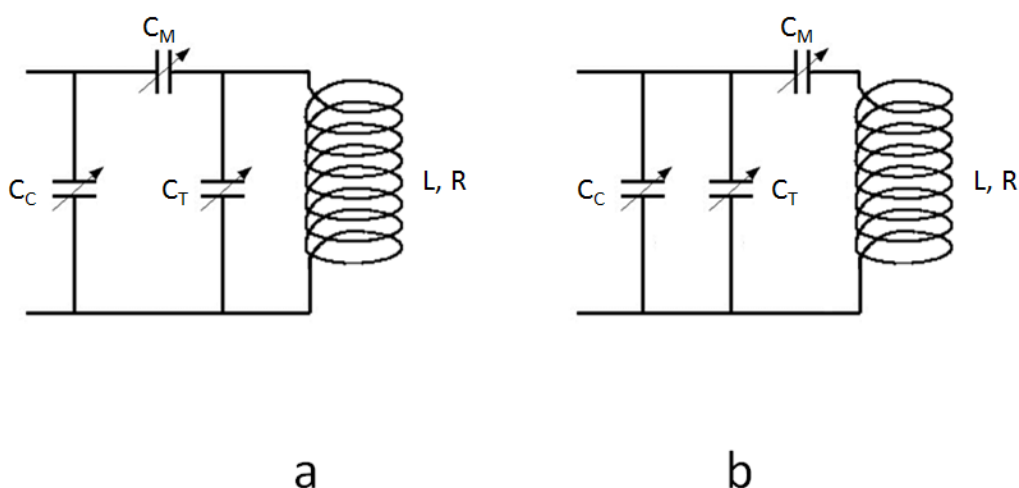


Figure C.1: Circuits scheme for low (a) and high (b) Larmor frequency nuclei

between the circuit and the pre-amplifier is achieved by matching the resultant impedance with $(50+0i) \Omega$ (see section 2.3.2). Thus our goal is to solve the following equations.

$$Z_{low} = \frac{1}{i\omega_L C_C + \frac{1}{\frac{1}{i\omega_L C_M} + \frac{1}{i\omega_L C_T + \frac{1}{i\omega_L L + R}}} = (50 + 0i)\Omega \quad (C.1)$$

$$Z_{high} = \frac{1}{i\omega_L C_C + i\omega_L C_T + \frac{1}{\frac{1}{i\omega_L C_M} + i\omega_L L + R}} = (50 + 0i)\Omega \quad (C.2)$$

While numerical solution of these equations is possible, it might become time consuming and built-in iterations of various programs often do not converge. Here, a purely mathematical simplification of these problems is suggested which is easy to implement.

C.1 Low frequency circuit

Without the additional capacitance of the semi-rigid cable, C_T would be the variable solely responsible for satisfying the real part of equation C.1 through a quadratic expression. From this point, expressing C_M by substituting C_T into the imaginary equation is easy. Introducing C_C makes the whole problem very complicated. However, assuming that the resultant impedance of the original circuit is a complex $a + bi$ the problem is simplified to the following equation.

$$Z_{low} = \frac{1}{i\omega_L C_C + \frac{1}{a+bi}} = (50 + 0i)\Omega \quad (C.3)$$

From which a and b are easily expressed as follows.

$$b = \frac{(50\Omega)^2 \omega_L C_C}{1 + (50\Omega)^2 \omega_L^2 C_C^2} \quad (C.4)$$

$$a = \sqrt{\frac{b(1 - b\omega_L C_C)}{\omega_L C_C}} \quad (C.5)$$

This means that impedance of the original circuit has to be matched with $a + bi$ instead of $(50+0i) \Omega$, which will lead to the following expressions.

$$C_T = \frac{L - \sqrt{L^2 - (1 - \frac{R}{a}) \left(L^2 + \frac{R^2}{\omega_L^2} \right)}}{\omega_L^2 L^2 + R^2} \quad (C.6)$$

$$C_M = \frac{1}{\omega_L \left(\frac{\omega_L C_T R^2 + (1 - \omega_L^2 C_T L) \omega_L L}{(1 - \omega_L^2 C_T L)^2 + (\omega_L C_T R)^2} - b \right)} \quad (C.7)$$

C.2 High frequency circuit

In this case, C_M is solely responsible for satisfying the real part of equation C.2 and is easily expressed. From this point, C_T is also easily expressed from the imaginary part of the equation.

$$C_M = \frac{1}{\omega_L(L\omega_L - \sqrt{50\Omega R - R^2})} \quad (\text{C.8})$$

$$C_T = \frac{\omega_L^2 LC_M - 1}{\omega_L^2 C_M \left(R^2 + \left(\omega_L L - \frac{1}{\omega_L C_M} \right)^2 \right)} \quad (\text{C.9})$$

Bibliography

- [1] John E. Enderby Kim D. Collins, George W. Neilson. Ions in water: Characterizing the forces that control chemical processes and biological structure. *Biophysical Chemistry*, 128:95–104, 2007.
- [2] Andreas A. Zavitsas. Properties of water solutions of electrolytes and nonelectrolytes. *J. Phys. Chem. B*, 105:7805–7817, 2001.
- [3] Vladimir I. Chizhik. NMR relaxation and microstructure of aqueous electrolyte solutions. *Molecular Physics*, 90:653–659, 1996.
- [4] Martin Muschol Avanish S. Parmar. Hydration and hydrodynamic interactions of lysozyme: Effects of chaotropic versus kosmotropic ions. *Biophysical Journal*, 97:590–598, 2009.
- [5] Esther Nachliel Ran Friedman and Menachem Gutman. Molecular dynamics of a protein surface: Ion-residues interactions. *Biophysical Journal*, 89:768–781, 2005.
- [6] L. M. Pegram and Jr. M. T. Record. Quantifying accumulation or exclusion of H⁺, HO⁻ and Hofmeister salt ions near interfaces. *Chemical Physics Letters*, 467:1–8, 2008.
- [7] Cremer PS Zhang Y. Interactions between macromolecules and ions: The Hofmeister series. *Current Opinion in Chemical Biology*, 10:658–663, 2006.
- [8] A. Abragam. *Principles of Nuclear Magnetism*. Oxford University Press, Oxford, England, 1961.
- [9] <http://mri-q.com/bloch-equations.html>, May 2014.
- [10] <http://www.mikepuddephat.com/Page/1603/>, May 2014.
- [11] <http://triton.iqfr.csic.es/guide/man/beginners/chap3-9.htm>, May 2014.

- [12] E. Fukushima and S. B. Roeder. *Experimental Pulsed NMR, a Nuts and Bolts Approach*. Westview Press, 1993.
- [13] L.A McLachlan. Lumped circuit duplexer for a pulsed NMR spectrometer. *Journal of Magnetic Resonance (1969)*, 39:11 – 15, 1980.
- [14] Paul C. Lauterbur Zhi-Pei Liang. *Principles of Magnetic Resonance Imaging*. SPIE Optical Engineering Press, New York, 2000.
- [15] http://commons.wikimedia.org/wiki/File:Nmr_fid_good_shim_EN.svg, May 2014.
- [16] <https://www.soils.org/publications/vzj/articles/9/4/893>, May 2014.
- [17] C. P. Slichter. *Principles of Magnetic Resonance*. Springer-Verlag, New York, 3rd ed. 1996 edition, 1989.
- [18] Villa Marco Massara Carla Isella Bjorkstam John L., Listerud John. Motional narrowing of a gaussian nmr line. *Journal of Magnetic Resonance (1969)*, 65:383–394, 1985.
- [19] Sture Forsen Bjorn Lindman. *Chlorine, Bromine and Iodine NMR. Physico-Chemical and Biological Applications*. Springer-Verlag, 1976.
- [20] A.P. Zens. NMR probe coil system, 1983. US Patent 4,398,149.
- [21] J. Mispelter, M. Lupu, and A. Briguet. *NMR Probeheads for Biophysical and Biomedical Experiments: Theoretical Principles and Practical Guidelines*. Imperial College Press, 2006.
- [22] <http://www.nature.com/nchem/journal/v3/n10/full/nchem.1143.html>, May 2014.
- [23] J. B. Johnson. Thermal agitation of electricity in conductors. *Phys. Rev.*, 32:97–109, 1928.
- [24] H. Nyquist. Thermal agitation of electric charge in conductors. *Phys. Rev.*, 32:110–113, 1928.
- [25] N. Bloembergen, E. M. Purcell, and R. V. Pound. Relaxation effects in nuclear magnetic resonance absorption. *Phys. Rev.*, 73:679–712, 1948.

- [26] J. Kestin and I.R. Shankland. Viscosity of aqueous NaCl solutions in the temperature range 25 - 200 °C and in the pressure range 0.1 - 30 MPa. *International Journal of Thermophysics*, 5:241–263, 1984.
- [27] http://www.scaweb.org/assets/papers/2005_papers/1-SCA2005-51.pdf, May 2014.
- [28] Yizhak Marcus. Viscosity B-coefficients of ions in solution. *Chem. Rev.*, 95:2695–2724, 1995.
- [29] <http://arxiv.org/ftp/arxiv/papers/0706/0706.1355.pdf>, May 2014.
- [30] Harald Schwalbe, Shaun B. Grimshaw, Andrew Spencer, Matthias Buck, Jonathan Boyd, Christopher M. Dobson, Christina Redfield, and Lorna J. Smith. A refined solution structure of hen lysozyme determined using residual dipolar coupling data. *Protein Science*, 10:677–688, 2001.